

Multiwavelength observations of the supernova remnant G349.7+02 interacting with a molecular cloud

J. S. Lazendic^{1,2}, M. Wardle³, J. B. Whiteoak⁴, M. G. Burton⁵ and A. J. Green¹

¹ School of Physics A28, University of Sydney, Sydney NSW 2006, Australia

² Harvard-Smithsonian Center for Astrophysics, 60 Garden Street, Cambridge, MA 02138, USA

³ Department of Physics, Macquarie University, NSW 2109, Australia

⁴ Australia Telescope National Facility, CSIRO, PO Box 76, Epping NSW 1710, Australia

⁵ School of Physics, University of New South Wales, Sydney NSW 2052, Australia

ABSTRACT

We present molecular-line observations at millimetre, centimetre and infrared wavelengths of the region containing OH(1720 MHz) masers in the supernova remnant (SNR) G349.7+0.2, using Australia Telescope (AT) Mopra antenna, Swedish-ESO Submillimeter Telescope, AT Compact Array and UNSW Infrared Fabry-Perot narrow-band filter in conjunction with the Anglo Australian Telescope. Several molecular transitions were observed between 1.6 and 3 mm to constrain the physical parameters of the molecular cloud interacting with the SNR and to investigate the effects of the SNR shock on the gas chemistry. The observed molecular-line profiles imply the presence of shocked gas with a density around 10^5 cm^{-3} and temperature around 30 K. Our measurements indicate that the abundances of molecular species such as CS, HCN and H₂CO are unaffected by the shocks, while HCO⁺, SO and SiO could be enhanced. We detected shock-excited near-infrared H₂ emission towards the centre of the SNR, revealing highly clumped molecular gas. An excellent correlation between the H₂ clumps and OH(1720 MHz) maser positions confirms the shock excitation of the OH(1720 MHz) maser emission. Furthermore, we detected OH absorption at 1665 and 1667 MHz which shows a good correlation with the shocked H₂ emission and the masers. We also found maser emission at 1665 MHz near the OH(1720 MHz) masers in this SNR, which could be excited by the shock-heated dust, evident in the mid-infrared wavelengths, or it could be pointing to an unrelated protostellar object along the line of sight to the remnant. We also detected 1665 and 1667 MHz OH masers towards the ultra-compact H II region IRAS 17147–3725 located to the southeast of the SNR. We found no 4.7- or 6-GHz excited-state OH masers or 6-GHz CH₃OH maser towards either the SNR or the H II region. Weak H₂CO absorption was detected only towards the H II region.

Key words: supernova remnants – ISM: clouds, masers, shock waves – individual: G349.7+0.2, IRAS 17147–3725 – infrared: ISM

1 INTRODUCTION

The young, massive stars which are progenitors of supernova remnants (SNRs) live only a relatively short time (a few million years) and have not moved far from the molecular clouds from which they are born. Hence it is expected that SNRs formed from such massive stars should be found in close proximity to parent molecular clouds. The shocks driven by SNRs into dense molecular clouds compress, accelerate and heat the gas. They can partially or completely disrupt the clouds and may also initiate star formation by triggering further gravitational collapse following the cooling

of the compressed gas. The shocks also provide energy which can potentially excite higher molecular transitions and activate chemical reactions forbidden in cold molecular clouds, changing the chemical abundances in the cloud. Thus, observations of molecular clouds which have encountered a supernova blast wave can provide important information about physical and chemical processes associated with the shocks.

Despite the expected association between SNRs and molecular clouds, very few unambiguous cases of interaction were known until recently. The best case was the SNR IC443, where an SNR-molecular cloud interaction was supported by the presence of broad molecular lines (DeNoyer 1979;

van Dishoeck, Jansen & Phillips 1993) and shocked molecular hydrogen (Burton et al. 1988). Establishing other specific cases has been difficult, mostly because of observational limitations. Although any interaction between a supernova blast wave and a molecular cloud will produce near-infrared (NIR) emission from shock-excited molecular hydrogen, surveying extended regions at NIR wavelengths is difficult because the fields of view of the telescopes at this wavelength are usually small. The fields of view at millimetre wavelengths are larger, but suffer confusion with unrelated clouds along the line of sight to an SNR, and the possibility of chance alignments.

OH(1720 MHz) maser emission, detected near the boundary regions of $\sim 10\%$ of the Galactic SNRs (Frail, Goss & Slysh 1994; Frail et al. 1996; Yusef-Zadeh et al. 1996; Green et al. 1997; Koralesky et al. 1998), is a convincing signpost of the SNR interaction with molecular clouds. This maser emission, usually unaccompanied by maser emission in the other three ground-state transitions, is excited by OH collisions with H₂ molecules in a gas with temperatures between 50–125 K, density of $\sim 10^5$ cm⁻³ and OH column density of $N(\text{OH})$ between 10^{15} and 10^{17} cm⁻² (Elitzur 1976; Lockett, Gauthier & Elitzur 1999). These conditions can be found in cooling gas behind a non-dissociative C shock, irradiated by the X-ray flux from the SNR interior (Wardle 1999). Thus SNRs associated with this maser emission are good candidates for studies of shock phenomena in molecular clouds. This has been supported by molecular-line observations of a few of these SNRs, which confirmed the presence of shocked molecular gas towards OH(1720 MHz) maser locations (Frail & Mitchell 1998; Reach & Rho 1999; Lazendic et al. 2002; Reach et al. 2002; Lazendic et al. 2004a).

One of the SNRs associated with OH(1720 MHz) maser emission is G349.7+0.2. This is the third brightest galactic SNR at radio wavelengths, after Cas A and the Crab Nebula (Shaver et al. 1985). It is classified as a shell-type remnant on the basis of radio continuum showing a circular shape, ~ 2.5 arcmin in diameter, with a bright periphery, and a typical spectral index of -0.5 (see e.g. Fig. 1 and associated discussion in Section 3.1). However, it has southern emission enhancement that differs from the uniform ring-brightness of typical shell-SNRs. Five OH(1720 MHz) masers have been detected along the bright emission ridge of the SNR (Frail et al. 1996) with radial LSR (local standard of rest) velocities ranging from 14.3 to 16.9 km s⁻¹; their properties are listed in Table 1. A magnetic field with strength of 0.35 ± 0.05 mG has been measured towards the brightest of the masers (Brogan et al. 2000). A distance of 18.3 ± 4.6 kpc has been estimated towards the SNR from the H I absorption (Caswell et al. 1975), and the maser velocities are consistent with this value (~ 22.4 kpc; Frail et al. 1996). The remnant has been studied in X-ray band with the *Advanced Satellite for Cosmology and Astrophysics* (Yamauchi et al. 1998; Slane et al. 2002) and the *Chandra X-ray Observatory* (Lazendic et al. 2004b).

To investigate the effects of SNR shocks on interstellar molecular gas and test the models for the shock origin of OH(1720 MHz) emission, we carried out molecular-line observations in radio and infrared bands. We used observations of molecular hydrogen to trace recently shocked gas identified by the presence of the masers. Molecular lines at mil-

limetre wavelengths are used to probe the structure, dynamics and composition of the molecular gas in which masers are created. OH line observations at centimetre wavelengths are used to derive OH column densities and test the model of OH(1720 MHz) maser production. We summarize the observations in Section 2, present the results in Section 3, discussed the results in Section 4, and provide our conclusions in Section 5.

2 OBSERVATIONS

2.1 Molecular-line observations at mm wavelengths

To obtain the initial distribution of the molecular cloud associated with G349.7+0.2 we used the 22 m Australia Telescope Mopra antenna during October 1998. The observations of the 3-mm 1–0 transition of ¹³CO were obtained in a 7×7 grid centred at RA(2000) = $17^{\text{h}} 18^{\text{m}} 00^{\text{s}}$, Dec.(2000) = $-37^{\circ} 26' 10''$, with a 30 arcsec grid and 60 second integration per position. For observations of other molecular species (¹²CO, CS, HCO⁺, HCN, H₂CO, SiO and SO) we used the 15 m Swedish-ESO Submillimetre Telescope (SEST) telescope during February and June 1999. The observed transitions, their frequencies and corresponding beam-widths are given in Table 2. Most of the transitions were observed over a 2×2.5 arcmin² region centred at RA(2000) = $17^{\text{h}} 18^{\text{m}} 00^{\text{s}}$, Dec.(2000) = $-37^{\circ} 26' 30''$, with a 24 arcsec grid spacing and 60 second integration per position. Due to the overall weak emission of CS, H₂CO, SO and SiO lower energy transitions, higher transitions for these species were observed only at the maser positions in a five-point cross grid with 20 arcsec offset. For all transitions a position-switching observing mode was used with a reference position at RA(2000) = $17^{\text{h}} 13^{\text{m}} 23^{\text{s}}$, Dec.(2000) = $-37^{\circ} 03' 30''$.

At the time of the ¹³CO Mopra antenna observations at 110 MHz, the effective diameter of the antenna was 15 m; the corresponding beam-width of about 43 arcsec was smaller than the SEST beam-width of about 45 arcsec for the 115-GHz ¹²CO observations. For the Mopra observations, the attenuation due to atmospheric absorption was corrected using the measurements of a black-body paddle at ambient temperature (see Hunt Cunningham et al. 2004, for more details). The corrected intensities were then matched to the main-beam temperature scale of the SEST by observing the molecular cloud in the direction of the Ori A SiO maser and scaling the observed intensities to their SEST counterparts. The final intensity calibration is believed to be accurate to within 15 per cent. The SEST observations were similarly corrected for atmospheric attenuation during the observations. For both telescopes the pointing was corrected approximately every 2 hours by observations of the 86 GHz SiO masers of AH Sco and W Hyd.

2.2 Near-infrared observations

The NIR observations were carried out during June 1999 using the University of New South Wales Infrared Fabry-Perot narrow-band filter (UNSWIRF; Ryder et al. 1998), in conjunction with the Infrared Imager and Spectrometer (IRIS; Allen et al. 1993) on the 3.9 m Anglo-Australian

Telescope (AAT). A pixel size of 0.77 arcsec resulted in a circular image of 100 arcsec in diameter. Observations were obtained in the $2.12\text{ }\mu\text{m}$ H_2 1–0 S(1) transition, centered at $\text{RA}(2000) = 17^{\text{h}} 17^{\text{m}} 58^{\text{s}}$, $\text{Dec.}(2000) = -37^{\circ} 26' 27''$, and $2.25\text{ }\mu\text{m}$ H_2 2–1 S(1) transitions, centered at a similar position. Each observation consisted of a set of five Fabry-Perot frames, equally spaced by 40 km s^{-1} , centred on the average maser velocity. The velocity resolution was $\approx 75\text{ km s}^{-1}$. The integration time was 180 seconds per frame for all observations. The data were reduced using modified routines in the **IRAF** software package (Ryder et al. 1998). An off-line frame, with velocity offset by -400 km s^{-1} from the first on-source frame, was taken for subsequent continuum subtraction. The intensity was calibrated using additional observations of the standard star BS 6441. Final data cubes were fitted with the instrumental Lorentzian profile to determine the line flux for the H_2 emission across the field. The final uncertainty in the line flux is less than 30 per cent. It should be noted that the line images obtained at different velocities are not true velocity channel maps, because velocities between the different frames are not independent. Both the central wavelength and the spectral resolution vary between pixels (in a reproducible manner) by up to $\approx 20\text{ km s}^{-1}$. We calibrated out these by measurement of an arc line, yielding line centre maps.

To establish the spatial coordinates for the H_2 image we obtained images with the Cryogenic Array Spectrometer Imager (CASPIR; McGregor et al. 1994) camera installed on the 2.3 m telescope at the Siding Spring Observatory during June 1999. The observations were undertaken using standard filters: J (1.15–1.4 μm), H (1.55–1.8 μm) and K (2.0–2.4 μm). The selected pixel size of 0.5 arcsec yielded individual frames with a size of ≈ 2 arcmin. A total of nine frames, with 20 arcsec spatial overlap, was obtained with each filter. The exposure time was 180 seconds for an individual frame. For each filter, bias and dark frames were taken, as well as frames of dome lamp light for flat-fielding. The data were reduced using modified routines in **IRAF**. No extended emission was detected and median sky frames were made by combining six neighboring source frames. To make the final image, the nine observed frames per filter were combined in a mosaic covering a region of $\approx 5 \times 5$ arcmin 2 . For the astrometry, stars in the J -band mosaic were matched with Digital Sky Survey (DSS) stars. Stars which were also detectable in the K -band mosaic were then used as reference stars for astrometry of the UNSWIRF frames. The absolute positions have a maximum uncertainty better than 1 arcsec.

2.3 Molecular-line observations at cm wavelengths

We used the Australia Telescope Compact Array (ATCA), which consists of six 22 m antennas (see Frater, Brooks & Whiteoak 1992, for more information), to observe ground- and excited-state transitions of OH at 1.6, 4.7 and 6.0 GHz, the 4.8 GHz transition of H_2CO and the 6.6 GHz transition of CH_3OH . The observational parameters are listed in Table 3 and the observed molecular transitions in Table 4. For some observations the correlator configuration also included a wide-band (128 MHz band over 32 channels) for observations of continuum emission in addition to the narrow spectral-line band (see Table 3). Amplitude calibrator PKS 1934–638 was observed at each

frequency to provide primary flux density and bandpass calibration. An observing cycle was used in which target source integrations were bracketed by short observations of phase calibrator PKS 1718–649 used for calibration of the complex antenna gains. For the ground-state OH transitions the observing band was centred at 1666 MHz to include emission from both ‘main’ lines at 1665 and 1667 MHz. The excited-state OH observations consisted of two or three contiguous 10-minute integrations on-source with the observing band set at the different transition frequencies for each integration. Line-free channels were used to subtract the continuum emission from all channels to form spectral-line data cubes and, in some cases, continuum images. The rms values for the final spectral-line cubes are listed in Table 3.

A continuum image at 18 cm was produced from two datasets at 1666 MHz formed by averaging about 350 of 1024 channels which were line-free. The continuum image at 6 cm was constructed by combining data at 6035 MHz and 4829 MHz. For the 6035 MHz observations the 128 MHz continuum band was used. However, for the 4829 MHz data, no H_2CO was detected and the central 1800 channels of the 4 MHz spectral band were used. Because of different pointing centres and central frequencies for the two datasets, we used mosaicing and multi-frequency synthesis techniques from the **MIRIAD** software package (Sault & Killeen 1997).

3 RESULTS AND ANALYSIS

3.1 SNR morphology

In Figure 1 we show the continuum images of G349.7+0.2 at 18 and 6 cm. The 18 cm image has a FWHM synthesized beam of $9.^{\circ}0 \times 5.^{\circ}8$ (P.A. = $-1^{\circ}0$), and an rms noise of 1.5 mJy beam^{-1} ; the image is similar to existing radio images of the region (Frail et al. 1996; Brogan et al. 2000). The final 6 cm image has a synthesised beam of $2.^{\circ}5 \times 1.^{\circ}8$ (P.A. = $-5^{\circ}7$) and an rms noise of 0.2 mJy beam^{-1} . Only the bright eastern part of the SNR was detected at 6 cm. The emission to the west is too weak to be detected at higher frequencies with the available sensitivity and resolution. As a consequence of the extent of the shortest array baselines used for observations, the 6 cm image is sensitive to structures ≤ 2 arcmin in size and the 18 cm image is sensitive to structures up to 5–8 arcmin in size. Smooth features which are larger than these angular sizes have been resolved out. The integrated flux densities of 15.5 and 6.6 Jy at 18 and 6 cm respectively, give a mean spectral index of -0.7 ± 0.3 between these two wavelengths. The spectral index shows possible variations over the brightest region of the SNR, with a flatter spectrum coinciding with the OH masers, but more sensitive observations are needed to confirm this trend. Similar flattening of the spectral index was found in W28, another SNR with OH(1720 MHz) masers, at the location where the SNR shell is encountering dense molecular gas, and this suggests that such interactions affect the energy spectrum of the relativistic particles (Dubner et al. 2000).

The influence of the interstellar medium on the radio morphology of G349.7+0.2 has been studied by Reynoso & Mangum (2001). They mapped the ^{12}CO 1–0 distribution around the SNR over an area of 38×38 arcmin 2

with a resolution of 54 arcsec, which we show in Figure 2. The molecular cloud associated with the SNR ('cloud 1') is a part of a complex that encompasses another cloud south-east of the SNR ('cloud 2'), which is coincident with the low-brightness radio continuum source designated as ultra-compact (UC) H II region IRAS 17147–3725 (Wood & Churchwell 1989; Bronfman, Nyman, & May 1996). Reynoso & Mangum suggested that the SNR morphology is influenced by the density gradient in the surrounding molecular gas, with the bright SNR shell encountering denser gas, and fainter SNR shell expanding in a lower density gas. X-ray morphology revealed with the *Chandra X-ray Observatory* supports this inference (Lazendic et al. 2004b).

3.2 Millimetre-line emission

Several CO clouds were detected along the line of sight to G349.7+0.2. Figure 3 shows a ^{12}CO 1–0 spectrum in the range -20 to $+40 \text{ km s}^{-1}$; there are features at -10 km s^{-1} , $+6$ and $+16 \text{ km s}^{-1}$. To identify the molecular cloud associated with the SNR, we have assumed that the cloud has a velocity close to the maser velocity, i.e., $+16 \text{ km s}^{-1}$. Figure 4 shows the molecular-line spectra in the velocity range -10 to $+40 \text{ km s}^{-1}$, obtained towards the peak position mentioned above or, in the case of CS 3–2 and H_2CO $2_{(1,1)} - 1_{(1,0)}$ transitions, towards M1. Since the ^{13}CO spectra taken with the Mopra telescope were obtained with different grid positions and intervals, the ^{13}CO 1–0 spectrum shown in Figure 4 is from the pointing (at $\text{RA}(2000) = 17^{\text{h}} 17^{\text{m}} 58\overset{\text{s}}{.}5$, Dec. (2000) = $-37^{\circ} 26' 10\overset{\text{s}}{.}1$) closest to the SEST peak position. All the spectra appear to have symmetric, Gaussian-like profiles, except the line profile of HCN 1–0 which shows all three hyperfine components and was fitted with three Gaussian profiles. The basic line parameters derived from the fit to the spectral profiles are summarised in Table 5. The spectra have centre velocities between 12.9 and 16.7 km s^{-1} , which is in good agreement with the OH maser velocities in Table 1. The line widths range from 2.7 to 6.5 km s^{-1} , with an average value of $\approx 4 \text{ km s}^{-1}$.

Figure 5 shows contours of velocity-integrated (10 – 20 km s^{-1}) ^{12}CO 1–0 emission obtained with the SEST overlaid on the 18 cm continuum image of the SNR. The molecular gas peaks at position $\text{RA}(2000) = 17^{\text{h}} 17^{\text{m}} 59\overset{\text{s}}{.}6$, Dec. (2000) = $-37^{\circ} 26' 32\overset{\text{s}}{.}0$, which is close to the position of maser M1. Molecular maps of ^{12}CO 2–1 emission, as well as ^{13}CO , HCO^+ and HCN emission (not shown), are remarkably similar to the ^{12}CO 1–0 map in Figure 5. For CS, H_2CO and SO observations, the emission was strongest towards M1. No emission was detected from SiO.

3.3 Properties of the molecular gas

The distribution of both the H₂ emission and OH absorption (see below) extends over $40 \times 90 \text{ arcsec}^2$, which implies that this is probably the true size of the cloud. In that case, the extent of the source is larger than the SEST beams and there is no beam dilution of the observed brightness temperature, only some loss of efficiency. The SEST beam-efficiency for extended objects (as measured by observations of the Moon) is 0.9 both at 100 and 230 GHz; using this value, we converted the observed brightness temperature of the two ^{12}CO

transitions to a main-beam brightness temperature, which is then used to derive the kinetic temperature of the molecular gas. A statistical-equilibrium excitation code supplied by J. H. Black (private communication) was employed to model the molecular line emission. The code uses a mean escape probability (MEP) approximation for radiative transfer (for more details see Jansen, van Dishoeck & Black 1994). For a given kinetic temperature and density of the gas, together with a total molecular column density and species line width, the code calculates the molecular line intensities, which can be compared with observed values. By plotting the ^{12}CO 2–1/1–0 line intensity ratio of ≈ 1.13 versus the ^{12}CO 2–1 line intensity, we derive kinetic temperature of the molecular gas $T_{\text{kin}} = 20$ – 40 K for a gas density of 10^4 – 10^6 cm^{-3} . The derived column density of ^{12}CO is 3.2×10^{16} – $2.0 \times 10^{17} \text{ cm}^{-2}$.

The ^{12}CO 2–1/1–0 line ratio of ≈ 1 and the $^{12}\text{CO}/^{13}\text{CO}$ 1–0 line ratio of ≈ 3.3 , both imply that the ^{12}CO emission is optically thick. The derived kinetic temperature then refers to the region from which the optically thick ^{12}CO emission arises, and might not be true for the entire molecular cloud. Using an overall ^{12}C to ^{13}C abundance ratio of 50 ± 20 (e.g., Langer & Penzias 1990), we estimate an upper limit on the ^{12}CO 1–0 optical depth of ≈ 15 , and ^{13}CO 1–0 optical depth of ≈ 0.3 . Similarly, using the isotope abundance ratio and ^{12}CO column density, we obtain a ^{13}CO column density of 6.4×10^{14} – $4.0 \times 10^{15} \text{ cm}^{-2}$.

To derive the density of the molecular cloud it is common to use molecular species with dipole moment larger than that of ^{12}CO , such as CS. Distribution of the CS 2–1 emission (not shown here) implies that CS emission arises from a much smaller region than the ^{12}CO emission, so we use the main-beam efficiency (0.74 at 98 GHz and 0.67 at 147 GHz) to derive a main-beam brightness temperature of the two CS lines. We use a source size of $\approx 35 \text{ arcsec}$ to correct the CS main-beam brightness temperatures for beam dilution. A beam-deconvolved source brightness temperature can be found from $T_S = T_{\text{mb}}(1 + \Omega_B/\Omega_S)$, where Ω_B and Ω_S are the beam and source solid angles, respectively (e.g., Jansen et al. 1994; Rohlf & Wilson 1996). Modelling the two CS transitions for kinetic temperatures of $\approx 30 \text{ K}$ implies a gas density of $n(\text{H}_2) = 4 \times 10^4$ – $2 \times 10^5 \text{ cm}^{-3}$. The CS column density is 1.6×10^{13} – $7.9 \times 10^{13} \text{ cm}^{-2}$.

For the estimation of a total column density of the molecular cloud associated with the SNR we use the standard fractional abundance of ^{12}CO relative to H₂ of 10^{-4} (e.g., Irvine, Goldsmith, & Hjalmarson 1987; van Dishoeck et al. 1993), which implies $N(\text{H}_2) \approx 1.2 \times 10^{21} \text{ cm}^{-2}$ (for the average value of ^{12}CO column density of $1.2 \times 10^{17} \text{ cm}^{-2}$). For other observed molecular species we used the relation for optically thin transitions (e.g., Rohlf & Wilson 1996):

$$N_l = 2.07 \times 10^3 \frac{g_l \nu^3}{g_u A_{ul}} \int T_S dv, \quad (1)$$

where g_i ($i = u, l$) is the number of states with the same energy ($g_i = 1 + 2i$), A_{ul} is the Einstein A -coefficient of spontaneous emission, and ν is the transition's frequency in GHz. Using this relation we derive the column densities for HCO^+ and HCN using a source size the same as that for ^{12}CO , and for SO using a source size the same as that for CS; the values are listed in Table 8.

3.4 H₂ emission

Figure 6 shows the velocity-integrated 1–0 and 2–1 S(1) H₂ line emission detected towards G349.7+0.2. The 1 σ noise in the 1–0 line is 6×10^{-6} erg s^{−1} cm^{−2} sr^{−1} and in the 2–1 line is 4×10^{-6} erg s^{−1} cm^{−2} sr^{−1}. The south-eastern part of the 2.12 μ m H₂ 1–0 S(1) emission is truncated by the instrumental field of view, but the whole extent of the emission can be determined from the 2.25 μ m H₂ 2–1 S(1) emission. The H₂ emission extends about 1.5 arcmin with a maximum width of 40 arcsec. It has a clumpy structure containing several peaks (knots), which are about 15 arcsec in size. The maser positions are in general located near these H₂ knots. The line fluxes of the knots are corrected for a minimum extinction of $A_K \approx 3$ mag because the source is located behind the Galactic centre; the values are summarised in Table 6 and the numbering of the knots is the same as the numbering of the masers. After correction for extinction, the intensity ratio of the 1–0 and 2–1 S(1) H₂ transitions is about 5–6. However, we note that because of the uncertainties in the absolute calibration at the two line frequencies, the derived line ratios may have a (constant) scaling factor error of up to 50%. There is a range of line centre velocities across the source, indicated in Figure 6. Most of the H₂ emission has a line centre velocity around -40 km s^{−1}. However, the emission from H₂ knots 1 and 3 peaks in the fourth frame with the line center velocity of $+40$ km s^{−1}, while the emission from knot 2 has a velocity of -20 km s^{−1}. The range of H₂ velocities encompasses the velocities of the OH(1720 MHz) masers. The velocity-integrated H₂ emission contours are superimposed on the 18-cm radio continuum greyscale image in Figure 7. We note that there is also a clump of H₂ emission coincident with the radio continuum peak, which is obvious in the 2–1 S(1) line image, but is cut off by the edge of the field of view in the 1–0 S(1) line image.

3.5 Search for OH maser emission

We have detected weak emission from the OH main-line masers at 1665 and 1667 MHz towards two locations in the observed field. The positions and flux densities of the sources are summarised in Table 7 and maser profiles are shown in Figure 8. One of the main-line masers, denoted MM(1), was found towards the SNR. Its position is closest (offset by 5 arcsec in RA and 1 arcsec in Dec) to that of maser M3 and maser emission was detected only in the 1665 MHz transition. The other maser, MM(2), was detected in both main-line transitions and is centred on the UC H_{II} region IRAS 17147–3725. The detection of an OH(1665 MHz) maser towards the OH(1720 MHz) maser site in an SNR is very intriguing and we discuss it in more detail in section §4.4.

Our search for the higher frequency maser lines was unsuccessful; the 1 σ rms values are listed in Table 3. The relationship between ground- and excited-state transitions of OH masers has been studied in detail in star-forming regions (SFRs) observationally and theoretically (see e.g., Gray, Field, & Doel 1992; MacLeod 1997; Pavlakis & Kylafis 1996, 2000, and references therein). Gray et al. (1992) proposed a correlation between masering at 1720 and 4765 MHz in warm gas ($T_{kin} > 100$ K), and between 1720 and 6035 MHz in cooler molecular gas, which was

confirmed using single dish observations (MacLeod 1997). Models by Pavlakis & Kylafis (1996, 2000) imply that OH transitions around 4.7 GHz are often only excited in gas with higher density ($> 10^6$ cm^{−3}) than that required to produce the 1720 MHz maser. Furthermore, the transitions at 6031 and 6035 MHz require a strong far-infrared (FIR) radiation field. A satellite-line maser at 6049 MHz is more likely to be found, but is expected to be very weak at densities $< 10^6$ cm^{−3} (Pavlakis & Kylafis 2000) and would probably lie below our detection limits. Our results are therefore consistent with the OH excitation models.

3.6 Search for CH₃OH maser emission

The CH₃OH masers are related to star-formation and are often found to co-exist with OH masers (e.g., Plambeck & Menten 1990; Phillips et al. 1998). We searched for the CH₃OH maser emission at 6.6 GHz towards the location of two OH main-line masers in the field of G349.7+0.2. Of particular interest was to investigate whether MM(1) maser has the CH₃OH maser counterpart in order to clarify its origin. However, we did not detect a CH₃OH maser towards either of the OH main-line masers; the 1 σ rms values are listed in Table 3. This indicates that either CH₃OH is not sufficiently abundant, or the local conditions (gas temperature, density, dust temperature) are such that only OH masers are favoured (Cragg, Sobolev, & Godfrey 2002).

3.7 OH absorption

The 1665 and 1667 MHz OH absorption profiles toward G349.7+0.2 are shown in Figure 9 in the velocity range -150 to $+70$ km s^{−1}, Hanning smoothed by 3 channels. Prominent features are present around -110 , -95 , -65 , -25 , -10 , $+6$ and $+16$ km s^{−1}. The 1665 MHz profile differs from the 1667 MHz profile in having an additional feature at -70 km s^{−1}. This feature originates from a bright maser located north-west of the SNR, outside the observed field of view. These features are also seen in H_I absorption (Caswell et al. 1975), and some of them (for which we have velocity coverage) are seen in our ¹²CO spectra, i.e., features at -10 , $+6$ and $+16$ km s^{−1}. The $+16$ km s^{−1} feature, which we associate with the SNR because of the common velocity with the OH(1720 MHz) masers, is partially blended with the $+6$ km s^{−1} feature. To investigate the distribution of the 16 km s^{−1} OH cloud, we produced velocity-integrated (10–20 km s^{−1}) images of OH absorption with a resolution of $15'' \times 12''$ (P.A. = $-3^\circ 2$), which was degraded from the best available resolution to improve the image sensitivity. The OH images are shown in Figure 10, overlaid on the 18 cm radio continuum image. The distribution of the OH cloud does not mirror the continuum emission, but appears as an elongated feature, 40' wide and 1.5' long, covering the region of the OH(1720 MHz) maser emission. We note that over the SNR region containing the masers the continuum level is sufficiently constant, which suggests that variations in OH absorption are indicative of variations in OH column density. The two peaks in the OH absorption distribution coincide with the M2 and M4 maser locations. The 1665 MHz distribution is more extended than that of 1667 MHz, and

there is indentation in OH absorption distribution around the MM(1) maser emission, whose compact distribution is also shown in Figure 10.

Optical depth maps $\tau = -\ln((T_L/T_C) + 1)$ were calculated from the spectral line channel maps, where T_L and T_C are the intensities of the spectral line and continuum maps, respectively. The values of the optical depth were calculated for regions with the continuum intensity larger than 25 mJy beam $^{-1}$ because of the poor signal-to-noise at lower continuum levels. We compare the optical depth profiles and the line-to-continuum ratio profiles towards the peak of the OH cloud in Figure 11. The optical depths are quite high, around 1.2–1.3. The relative intensities of the OH absorption in the 1667 MHz and 1665 MHz lines are expected to have ratio around 9/5 for an optically thin gas in local thermal equilibrium (LTE). The line ratio T_{1667}/T_{1665} in G349.7+0.2 is ~ 1.1 , which differs significantly from the LTE value of 1.8, and is probably a result of the high optical depths of the OH transitions. OH absorption is typically observed with low optical depths, but higher optical depths have been found towards some SNRs (e.g. Yusef-Zadeh, Wardle, & Roberts 2003).

The OH column density for the LTE case can be obtained from (e.g., Crutcher 1977):

$$N(1665 \text{ MHz}) = 4.2 \times 10^{14} T_{ex} \int \tau_v dv \text{ cm}^{-2}, \quad (2)$$

$$N(1667 \text{ MHz}) = 2.3 \times 10^{14} T_{ex} \int \tau_v dv \text{ cm}^{-2}. \quad (3)$$

Modelling of OH level populations imply that for $T_{kin} \geq 20$ K an OH excitation temperature of 10 K is plausible (Yusef-Zadeh, Wardle, & Roberts 2003). Using the above values of the optical depth, we derive a peak OH column density of $(2.8\text{--}4.7) \times 10^{15} \text{ cm}^{-2}$. These values are consistent with the models of OH(1720 MHz) excitation (Elitzur 1976; Lockett et al. 1999) and with the model of OH production in C-type SNR shocks (Wardle 1999). These column densities also imply that the masers must be in front of the radio continuum, otherwise there would be less OH column from the absorption, and more from the masers if they were behind.

3.8 H₂CO absorption

H₂CO absorption at 4829 MHz is readily found in H II–molecular cloud complexes, where H II regions are embedded in dense molecular regions. There have been only a few such absorption detections towards SNRs (e.g., Whiteoak & Gardner 1974; Slysh et al. 1980; DeNoyer 1983), where the associated continuum emission, and consequently absorption against this emission, is usually much fainter than for H II regions. We did not detect H₂CO absorption towards G349.7+0.2, but we did find weak absorption towards the nearby UC H II region, with an optical depth of ≈ 1 and column density of $\approx 4.3 \times 10^{15} \text{ cm}^{-2}$ (for an adopted excitation temperature of 10 K and line width of 5 km s $^{-1}$). Using a 3σ upper limit towards the SNR and a line-width of 5 km s $^{-1}$, we estimate an optical depth < 0.013 and an H₂CO column density $< 1.7 \times 10^{13} \text{ cm}^{-2}$.

4 DISCUSSION

4.1 Shocked molecular gas associated with G349.7+0.2

The parameters derived for the molecular cloud associated with G349.7+0.2, $T_{kin} = 20\text{--}40$ K and $n(\text{H}_2) = 4 \times 10^4\text{--}2 \times 10^5 \text{ cm}^{-3}$, are consistent with values required for the production of OH(1720 MHz) masers by shock excitation (Lockett et al. 1999). The gas temperature is slightly lower than the 50–125 K required, but it refers just to the colder envelope of the cloud, so the temperature within the cloud is probably higher. Therefore, we detected shocked molecular gas produced by an expansion of G349.7+0.2 into a nearby molecular cloud. The parameters of the shocked molecular gas are similar to those found in SNR IC 443 (van Dishoeck et al. 1993). However, the millimetre-line widths of $\approx 4 \text{ km s}^{-1}$ are smaller than those found in one of the shock components in IC 443 ($\geq 10 \text{ km s}^{-1}$). Although the shock front containing the OH(1720 MHz) masers will be seen mostly perpendicular to the line-of-sight (hence showing minimal line broadening), some broadening is expected due to deflection of the shock directions in clumpy pre-shock gas (Turner & Lubowich 1991). High-velocity line wings were not detected in the low lying ¹²CO transitions, but may be too weak for detection with the short integration time used here.

In Table 8 we list molecular column densities and abundances determined using the H₂ column densities of $1.2 \times 10^{21} \text{ cm}^{-2}$, derived in section §3.3. Because the telescope beams are relatively large compared with the scale of the SNR, we were not able to observe the contributions from ambient and post-shock gas separately and thus are not able to compare post- and pre-shock abundances in the cloud associated with G349.7+0.2. Nevertheless, we attempted to compare our observed values with those of the SNR IC 443 from van Dishoeck et al. (1993), which is the only SNR to date where shock chemistry has been studied in great detail. We also compared them with abundances in dark clouds L134N and TMC-1 (Ohishi, Irvine, & Kaifu 1992), also used for comparison with IC 443 (van Dishoeck et al. 1993). Abundances in dark clouds provide information about basic molecular formation in gas-phase chemistry without contamination by ultraviolet (UV) photons from embedded sources. We find that the abundances of CS and HCN are comparable in SNRs and dark clouds. In other words, they remain unchanged for shocked gas, as expected from the models.

SiO is the only molecule in IC 443 found to have an abundance enhanced with respect to dark clouds (van Dishoeck et al. 1993). Observations and theoretical modelling indicate that in dark clouds Si is heavily depleted as it freezes out onto grains. Si-species like SiO become observable in warmer regions with temperatures higher than 30 K (Ziurys, Friberg, & Irvine 1989; Mackay 1996). Shock models predict enhanced SiO abundances as a product of gas-phase chemistry when Si is released from grains by evaporation or disruption from fast dissociative shocks (Neufeld & Dalgarno 1989; Mackay 1996; Schilke et al. 1997). This is supported by observations of young bipolar outflows where jets from a central star interact with ambient molecular gas (e.g., Garay et al. 1998). We did not detect SiO towards G349.7+0.2, and we estimate an

upper limit to its column density of $X(\text{SiO}) < 2 \times 10^{-8}$. This means that SiO could still be significantly enhanced with respect to dark clouds for which Ziurys et al. (1989) derived an upper limit of $X(\text{SiO}) \sim 4 \times 10^{-12}$.

Another molecule predicted to be enhanced in shocks is SO, and this enhancement depends on the H/H₂ ratio, the C/CO ratio, and on the initial form (atomic or molecular) of sulphur (see van Dishoeck et al. 1993, and references therein). Pineau Des Forets et al. (1993) suggested that SO can be found up to distances of 10^{18} cm from the shock front. The telescope beam at the observed SO frequency is such that we would expect beam dilution to render an SO enhancement undetectable, unless it is extended over substantial distances. The derived SO abundance of $\approx 1 \times 10^{-7}$ is greater than in the two dark clouds, and therefore we conclude that SO is enhanced in G349.7+0.2.

Early observations reported an enhancement of HCO⁺ towards IC 443 (Dickinson et al. 1980; DeNoyer & Frerking 1981), which was contrary to predictions for slow shocks (Iglesias & Silk 1978), but could be explained by the increased ionisation expected in SNRs (Elitzur 1983). However, later observations found that the HCO⁺ abundance in IC 443 was unaffected by the SNR shock (Ziurys et al. 1989) and even decreased in the high density gas, probably due to more rapid dissociative recombination with electrons and reactions with H₂O (van Dishoeck et al. 1993). Our result of 9.8×10^{-8} implies that the HCO⁺ abundance is either enhanced in G349.7+0.2, or that that the source size used for the HCO⁺ data was incorrect.

4.2 Shocked H₂

The measured H₂ 1–0/2–1 line ratio of 5–6 is somewhat lower than the ratio of 10–20 expected in C-shocks (Burton et al. 1988). A lower line ratio can be produced in J-shocks where the vibrational ground-states of H₂ are produced by a cascade following collisional excitation of excited electronic states. However, this type of shock cannot account for the high 1–0 S(1) line intensities observed in G349.7+0.2 (Hollenbach & McKee 1989). A very low line ratio (≈ 2) can be found in fluorescent H₂ emission produced by radiative excitation of low density gas by UV photons (Black & Dalgarno 1976). UV excitation can produce higher line ratios in molecular gas of density 10^5 – 10^6 cm^{−3} (Burton, Hollenbach, & Tielens 1990b). However, to produce 1–0 S(1) emission with a line peak of 0.005 erg s^{−1} cm^{−2} sr^{−1}, as found in G349.7+0.2, the far-UV radiation field needs to be more than 10^5 G₀, where G₀ represents the FUV radiation field equivalent to 1.6×10^{-3} erg s^{−1} cm^{−2} sr^{−1} (Burton et al. 1990b). This is unusually high to be produced by only a few young stars. For example, early-type B stars typically produce a field of $\approx 10^3$ G₀ (note that in the strict case this is a function of the distance from the star). Burton et al. (1990b) showed that less than 10^{-4} of the energy in 6–13.6 eV photons is re-emitted in the 1–0 S(1) line. The total NIR H₂ 1–0 S(1) line luminosity of G349.7+0.2 is about $500 L_\odot$ (see Table 6), so an exciting source would have to emit $5 \times 10^6 L_\odot$ in 6–13.6 eV photons. Its bolometric luminosity would be even higher. The H₂ emission we detect is too bright and extensive to be produced by UV excitation from a star, and despite the lower-than-expected line ratio, must be produced

by the SNR shock. Thus, it seems likely that the slightly low ratios measured for the 1–0/2–1 S(1) lines for this mechanism simply arises from an error in the absolute calibration of one or both of these lines.

There is also morphological evidence that the H₂ emission is related to the SNR shock. Figure 7 shows that the H₂ filament coincide with the western edge of the bright continuum SNR shell. The H₂ knots are associated with the locations of OH(1720 MHz) masers which are produced by collisional excitation. This morphological coincidence between the H₂ and radio continuum emission, and between the H₂ and maser emission suggest that all these phenomena are shock-related.

In shocks the 1–0 S(1) line contributes typically 5–10 per cent of the total H₂ luminosity (e.g., see Burton 1992). The H₂ luminosity of the source is therefore high, $\approx 5 \times 10^3 L_\odot$ at the distance of 18 kpc. This is about a factor of five higher than the $\approx 1 \times 10^3 L_\odot$ emitted in H₂ lines by the SNR IC 443 (Burton et al. 1988). It is also brighter than the extended fluorescent H₂ line emission associated with several massive star-forming complexes (e.g., $300 L_\odot$ from the PDR emission around the Orion Molecular Cloud-One; Burton & Puxley 1990).

4.3 Shocked OH?

Figure 12 shows contours of velocity-integrated OH absorption at 1667 MHz overlaid on the contours of velocity-integrated H₂ emission. Good correlation between OH and H₂ distribution suggests that the H₂ emission occurs in front of the radio continuum. Since H₂ is shock excited, this correlation is also a strong indication that the OH gas is produced in the shocked regions. Another support for shock origin is the association of OH peaks with the masers. The OH column density derived in section §3.7 yields an OH fractional abundance of $(2.3\text{--}3.9) \times 10^{-6}$, indicating that OH abundance in G349.7+0.2 is an order of magnitude higher than in dark clouds (e.g., $\sim 3 \times 10^{-7}$; Ohishi et al. 1992). An enhanced OH abundance towards an SNR (IC 443) was first reported by DeNoyer (1979), but shock models do not predict such an enhancement (Draine, Roberge, & Dalgarno 1983; Hollenbach & McKee 1989; Kaufman & Neufeld 1996). This is because for temperatures above 400 K, any OH formed will be rapidly converted into H₂O through reactions with H₂. However, X-rays from the interior of the remnant can penetrate the surrounding molecular cloud and eject photoelectrons, which then collisionally excite the Werner Ly α band of H₂, providing enough energy to dissociate H₂O back into OH, but not enough to dissociate OH (Wardle 1999). The process of forming OH occurs when the temperature has dropped so that the conversion of OH back into H₂O ceases. A warm, dense layer rich in OH develops at the back of the shock, which is ideal for the collisional pumping of the OH(1720 MHz) masers. The upper value of the derived OH abundance in G349.7+0.2 is consistent with predictions for the dissociation of 1 percent of the water by the SNR X-ray flux (Wardle 1999).

4.4 Maser emission and shock heated dust?

Main-line OH masers at 1665 and 1667 MHz are commonly used to study star-formation regions and are not expected to

be found at the sites of OH(1720 MHz) SNR masers. MM(2) is associated with the UC H_{II} region and thus is related to star-formation, but MM(1) may have a different origin. This maser emission could be related to the OH(1720 MHz) emission or it could originate from an H_{II} region with a radio continuum much fainter than that of the SNR and thus is not distinguishable from it. For example, the UC H_{II} region IRAS 17147–3725 has a brightness comparable with the lowest level of emission from the SNR.

To investigate this in more detail, we examined the available IR data towards G349.7+0.2. In Figure 13 we plot the locations of the newly OH detected main-line masers and the unresolved *IRAS* sources in the field. A source IRAS 17146–3723, designated as unresolved in the *IRAS* catalogue, is located ≈ 15 arcsec away from MM(1). However, note that the angular resolution for the *IRAS* observations ranges from 0.5–2 arcmin between 12 and 100 μ m. After estimating that the SNR is too young to have triggered star formation, Reynoso & Mangum (2001) suggested that this *IRAS* source originates from dust heated by the SNR shock rather than from a protostellar object. For confirmation, we obtained 8.3 and 21.3 μ m emission from the *Midcourse Space Experiment (MSX)* Galactic plane survey (Price et al. 2001), with a resolution of 20 arcsec, shown also in Figure 13. IRAS 17147–3725 has the typical morphology of an UC H_{II} region in both *MSX* bands (see e.g., Cohen & Green 2001). The *MSX* emission towards G349.7+0.2 coincides with the shocked part of the molecular gas, as shown in Figure 14, which suggests that mid-IR and far-IR emission are related to the SNR shock, and could indeed originate from warm dust collisionally heated by the SNR shock. It is also possible that this emission is dominated by radiation from lines rather than dust (i.e. continuum emission), as demonstrated in the case of IC 443, where far-IR morphology also traces that of shocked H₂ (Burton et al. 1990a; Oliva et al. 1999; Cesarsky et al. 1999).

The presence of an FIR radiation field would favour the masering of the 1665 and 1667 MHz transitions at the expense of the 1720 MHz transition. However, the OH(1665 MHz) maser towards G349.7+0.2 does not overlap in velocity or position with any of the OH(1720 MHz) masers, and this situation has also been found to occur in star-forming regions (e.g., Mashededer et al. 1994; Caswell 1999). The different locations for different masers may reflect differences in their formation requirements. OH excitation models show that a weaker 1665 MHz maser will co-exist with a 1720 MHz maser if the dust temperature is ≥ 100 K (Pavlakis & Kylafis 1996; Cragg et al. 2002). Indeed, using the *IRAS* flux Arendt (1989) derived a dust temperature of $40 < T_{\text{dust}} < 140$ K in G349.7+0.2, although this estimate would be invalid if the *IRAS* flux has a substantial contribution from the line component. However, for the gas temperature and density required to produce the SNR-type 1720 MHz maser, dust temperatures larger than 50 K will significantly suppress the inversion of the 1720 MHz emission (Lockett et al. 1999). Therefore, if the 1665 MHz maser is related to the SNR, it probably originates from a molecular clump with different physical conditions than those producing OH(1720 MHz) masers. A search at sub-millimetre wavelengths for a protostellar object might be able to resolve the nature of the MM(1) maser.

5 CONCLUSION

Radio and infrared observations towards the SNR G349.7+0.2, for which OH(1720 MHz) masers have been detected, were used to investigate the interaction of the SNR with the adjacent molecular cloud. The main results are summarised below.

(1) Emission from several molecular species (¹²CO, ¹³CO, CS, HCO⁺, HCN, H₂CO and SO) have been detected towards the SNR at the OH(1720 MHz) maser velocities. The molecular lines have moderate line widths (≈ 4 km s^{−1}), showing no kinematic evidence of shock. The gas temperature of 20–40 K is derived for the optically thick part of the cloud, implying that the true temperature of the cloud is higher. This fact and the gas density of 4×10^4 – 2×10^5 cm^{−3} imply the presence of shocked molecular gas. These values are also consistent with the predictions for OH(1720 MHz) maser production.

(2) Molecular abundances of the shocked molecular gas in G349.7+0.2 are found to be somewhat different than those in another well-studied SNR, IC 443. The abundances of molecules such as CS, HCN and H₂CO are not enhanced by the effect of the shock, as expected from the most plausible models. The abundances of HCO⁺ and SO appear to be enhanced in respect to dark clouds. No SiO emission was detected, but the upper limit to the SiO column density indicates a possibility of an enhanced SiO abundance.

(3) Strong H₂ emission was detected towards the SNR. Its distribution coincides with the radio continuum and the location of OH masers, supporting the notion that the H₂ emission arises from the SNR shock expanding into the adjacent molecular cloud. The total H₂ line luminosity in the source is very large, $\approx 5 \times 10^3 L_{\odot}$. It indicates that the interaction of SNRs with molecular clouds can produce H₂ line emission that is greater than that associated with fluorescent emission around massive star-forming complexes. This should be born in mind when interpreting extragalactic H₂ line emission.

(4) In G349.7+0.2 we have a clear observational evidence of extended OH cloud related to shocked regions in SNRs. The distribution of the OH gas correlates well with the OH(1720 MHz) maser locations and the distribution of shocked H₂. The value of OH fractional abundance ($\sim 10^{-6}$) is greater than in cold clouds and is consistent with predictions for water dissociation by soft X-ray flux from SNRs. We found no H₂CO absorption towards the SNR.

(5) We detected for the first time OH main-line maser emission at 1665 and 1667 MHz in direction towards or near G349.7+0.2. One of these main-line masers was found towards the SNR and was detected only in the 1665 MHz transition. The nature of this maser is not clear and further observations are needed to establish whether it is related to the SNR cloud or to a possible protostellar object along the line of sight. The other maser was detected in both main-line transitions and is centred on the ultra-compact H_{II} region IRAS 17147–3725 located south-east of the SNR. We also found weak H₂CO absorption towards this H_{II} region. No masering was found in the field towards the SNR in excited-state OH transitions near 5 and 6 GHz, or in the 6 GHz CH₃OH transition.

ACKNOWLEDGMENTS

We thank John Black for kindly providing us with his MEP code, Estela Reynoso for use of the 12-m NRAO CO map, Andrew Walsh for help with the CASPIR observations and Martin Cohen for useful discussions on the *MSX* data. JSL was supported by an Australian Government International Postgraduate Research Scholarship, a Sydney University Postgraduate Scholarship, and an ATNF Postgraduate Scholarship. JSL and JBW acknowledge travel support from the Australian Government's Access to Major Research Facilities Program (AMRFP). This work was also supported in part by the Australian Research Council.

The Australia Telescope Compact Array and Mopra Telescope are part of the Australia Telescope funded by the Commonwealth of Australia for operation as a National Facility, managed by CSIRO. The Swedish-ESO Submillimetre Telescope (SEST) is operated by the Swedish National Facility for Radio Astronomy, Onsala Space Observatory and by the European Southern Observatory (ESO). The NIR observations would not have been possible without the efforts of Michael Ashley and the UNSWIRF crew from UNSW, as well as the staff of the Anglo Australian Observatory. CASPIR is operated by the Australian National University at the 2.3 m telescope at Siding Spring Observatory. This publication makes use of data products from: (1) the Digitized Sky Surveys (DSS) were produced at the Space Telescope Science Institute under U.S. Government grant NAG W-2166. The images of these surveys are based on photographic data obtained using the Oschin Schmidt Telescope on Palomar Mountain and the UK Schmidt Telescope. The plates were processed into the present compressed digital form with the permission of these institutions. The National Geographic Society-Palomar Observatory Sky Atlas (POSS-I) was made by the California Institute of Technology with grants from the National Geographic Society; and (2) the NASA/IPAC Infrared Science Archive is operated by the Jet Propulsion Laboratory, California Institute of Technology, under contract with the National Aeronautics and Space Administration.

REFERENCES

Allen, D. A. et al. 1993, Proceedings of the Astronomical Society of Australia, 10, 298

Arendt, R. G. 1989, ApJS, 70, 181

Black, J. H. & Dalgarno, A. 1976, ApJ, 203, 132

Brogan, C. L., Frail, D. A., Goss, W. M., & Troland, T. H. 2000, ApJ, 537, 875

Bronfman, L., Nyman, L., & May, J. 1996, A&AS, 115, 81

Burton, M. G., Geballe, T. R., Brand, P. W. J. L., & Webster, A. S. 1988, MNRAS, 231, 617

Burton, M. G., Hollenbach, D. J., Haas, M. R., & Erickson, E. F. 1990a, ApJ, 355, 197

Burton, M. G., Hollenbach, D. J., & Tielens, A. G. G. M. 1990b, ApJ, 365, 620

Burton, M. & Puxley, P. J. 1990, in The Interstellar Medium in External Galaxies: Summaries of Contributed Papers p 238-240 (SEE N91-14100 05-90), 238

Burton, M. G. 1992, Australian Journal of Physics, 45, 463

Caswell, J. L., Murray, J. D., Roger, R. S., Cole, D. J., & Cooke, D. J. 1975, A&A, 45, 239

Caswell, J. L. 1999, MNRAS, 308, 683

Cesarsky, D., Cox, P., Pineau des Forets, G., van Dishoeck, E. F., Boulanger, F., & Wright, C. M. 1999, A&A, 348, 945

Cohen, M. & Green, A. J. 2001, MNRAS, 325, 531

Cragg, D. M., Sobolev, A. M., & Godfrey, P. D. 2002, MNRAS, 331, 521

Crutcher, R. M. 1977, ApJ, 216, 308

DeNoyer, L. K. 1979, ApJL, 228, L41

DeNoyer, L. K. & Frerking, M. A. 1981, ApJL, 246, L37

DeNoyer, L. K. 1983, ApJ, 264, 141

Dickinson, D. F., Dinger, A. S. C., Kuiper, T. B. H., & Rodriguez Kuiper, E. N. 1980, ApJL, 237, L43

Draine, B. T., Roberge, W. G., & Dalgarno, A. 1983, ApJ, 264, 485

Dubner, G. M., Velázquez, P. F., Goss, W. M., & Holdaway, M. A. 2000, AJ, 120, 1933

Elitzur, M. 1976, ApJ, 203, 124

Elitzur, M. 1983, ApJ, 267, 174

Fich, M., Blitz, L., & Stark, A. A. 1989, ApJ, 342, 272

Frail, D. A., Goss, W. M. & Slysh, V. I. 1994, ApJL, 424, L111

Frail, D. A., Goss, W. M., Reynoso, E. M., Giacani, E. B., Green, A. J. & Otrupcek, R. 1996, AJ, 111, 1651

Frail, D. A. & Mitchell, G. F. 1998, ApJ, 508, 690

Frater, R. H., Brooks, J. W., & Whiteoak, J. B. 1992, Journal of Electrical and Electronics Engineering Australia, 12, 103

Garay, G., Köhnenkamp, I., Bourke, T. L., Rodríguez, L. F., & Lehtinen, K. K. 1998, ApJ, 509, 768

Gray, M. D., Field, D., & Doel, R. C. 1992, A&A, 262, 555

Green, A. J., Frail, D. A., Goss, W. M. & Otrupcek, R. 1997, AJ, 114, 2058

Hollenbach, D. & McKee, C. F. 1989, ApJ, 342, 306

Hunt Cunningham, M., Whiteoak, J. B., Jones, P. A., & White, G. L. 2004, submitted to MNRAS (astro-ph/0312442)

Iglesias, E. R. & Silk, J. 1978, ApJ, 226, 851

Irvine, W. M., Goldsmith, P. F., & Hjalmarson, A. 1987, ASSL Vol. 134: Interstellar Processes, 561

Jansen, D. J., van Dishoeck, E. F. & Black, J. H. 1994, A&A, 282, 605

Kaufman, M. J. & Neufeld, D. A. 1996, ApJ, 456, 611

Koralesky, B., Frail, D. A., Goss, W. M., Claussen, M. J., & Green, A. J. 1998, AJ, 116, 1323

Langer, W. D. & Penzias, A. A. 1990, ApJ, 357, 477

Lazendic, J. S., Wardle, M., Burton, M. G., Yusef-Zadeh, F., Whiteoak, J. B., Green, A. J., & Ashley, M. C. B. 2002, MNRAS, 331, 537

Lazendic, J. S., Wardle, M., Burton, M. G., Yusef-Zadeh, F., Green, A. J., Whiteoak, J. B. 2004a, submitted to MNRAS

Lazendic, J., Slane, P., Chen, Y., Hughes, J. P., & Dame, T. 2004b, submitted to ApJ

Lockett, P., Gauthier, E. & Elitzur, M. 1999, ApJ, 511, 235

Mackay, D. D. S. 1996, MNRAS, 278, 62

MacLeod, G. C. 1997, MNRAS, 285, 635

Masheder, M. R. W., Field, D., Gray, M. D., Migenes, V., Cohen, R. J., & Booth, R. S. 1994, A&A, 281, 871

McGregor, P., Hart, J., Downing, M., Hoadley, D., & Bloxham, G. 1994, Experimental Astronomy, 3, 139

Neufeld, D. A. & Dalgarno, A. 1989, ApJ, 340, 869

Ohishi, M., Irvine, W. M., & Kaifu, N. 1992, IAU Symp. 150: Astrochemistry of Cosmic Phenomena, 150, 171

Oliva, E., Lutz, D., Drapatz, S., & Moorwood, A. F. M. 1999, A&A, 341, L75

Pavlakis, K. G. & Kylafis, N. D. 1996, ApJ, 467, 309

Pavlakis, K. G. & Kylafis, N. D. 2000, ApJ, 534, 770

Phillips, C. J., Norris, R. P., Ellingsen, S. P., & McCulloch, P. M. 1998, MNRAS, 300, 1131

Pineau Des Forets, G., Roueff, E., Schilke, P., & Flower, D. R. 1993, MNRAS, 262, 915

Plambeck, R. L. & Menten, K. M. 1990, ApJ, 364, 555

Price, S. D., Egan, M. P., Carey, S. J., Mizuno, D. R., & Kuchar, T. A. 2001, AJ, 121, 2819

Reynoso, E. M. & Mangum, J. G. 2001, AJ, 121, 347

Reach, W. T. & Rho, J. 1999, ApJ, 511, 836

Reach, W. T., Rho, J., Jarrett, T. H., & Lagage, P. 2002, ApJ, 564, 302

Rohlfs, K. & Wilson, T. L. 1996, *Tools of Radio Astronomy*, Springer-Verlag, Berlin

Ryder, S. D., Sun, Y.-S., Ashley, M. C. B., Burton, M. G., Allen, L. E. & Storey, J. W. V. 1998, Publications of the Astronomical Society of Australia, 15, 228

Sault, R. J. & Killeen, N., 1997, 'Miriad Users Guide,' ATNF Publication

Shaver, P. A., Salter, C. J., Patnaik, A. R., van Gorkom, J. H., & Hunt, G. C. 1985, Nature, 313, 113

Schilke, P., Walmsley, C. M., Pineau Des Forets, G., & Flower, D. R. 1997, A&A, 321, 293

Slane, P., Chen, Y., Lazendic, J. S., & Hughes, J. P. 2002, ApJ, 580, 904

Slysh, V. I., Wilson, T. L., Pauls, T., & Henkel, C. 1980, IAU Symp. 87: Interstellar Molecules, 87, 473

Stanimirović, S., Weisberg, J. M., Dickey, J. M., de la Fuente, A., Devine, K., Hedden, A., & Anderson, S. B. 2003, ApJ, 592, 953

Turner, B. E. & Lubowich, D. A. 1991, ApJ, 381, 173

van Dishoeck, E. F., Jansen, D. J., & Phillips, T. G. 1993, A&A, 279, 541

Wardle, M. 1999, ApJL, 525, L101

Whiteoak, J. B. & Gardner, F. F. 1974, A&A, 37, 389

Wood, D. O. S. & Churchwell, E. 1989, ApJ, 340, 265

Yamauchi, S., Koyama, K., Kinugasa, K., Torii, K., Nishiochi, M., Kosuga, T., & Kamata, Y. 1998, Astronomische Nachrichten, 319, 111

Yusef-Zadeh, F., Roberts, D. A., Goss, W. M., Frail, D. A. & Green, A. J. 1996, ApJL, 466, L25

Yusef-Zadeh, F., Wardle, M., & Roberts, D. A. 2003, ApJ, 583, 267

Ziurys, L. M., Friberg, P., & Irvine, W. M. 1989, ApJ, 343, 201

Table 1. The OH(1720 MHz) masers detected towards the SNR G349.7+0.2 (from Frail et al. 1996).

Designation	RA(2000) (h m s)	Dec.(2000) ($^{\circ}$ ' '')	S_p (mJy)	V_{LSR} (km s^{-1})	Δv (km s^{-1})
M1	17 17 59.2	-37 26 21.07	90	+16.7	1.5
M2	17 17 59.2	-37 26 48.07	152	+14.3	1.8
M3	17 17 59.9	-37 26 09.01	1310	+16.0	1.8
M4	17 18 00.9	-37 25 59.94	1020	+15.2	1.6
M5	17 18 01.4	-37 26 23.90	277	+16.9	1.4

Table 2. Mopra and SEST observational parameters for G349.7+0.2.

Parameter	Mopra	SEST
Observed frequencies (GHz)	110	86 – 270
Total bandwidth (MHz)	64	2×64
No. of frequency channels	1024	2×1000
Velocity resolution (km s^{-1})	0.20	0.06 – 0.14
Velocity coverage (km s^{-1})	160	60 – 100
FWHP beamwidth (arcsec)	43	57–20
Area observed (arcmin^2)	3.5×4	1.5×2
Grid interval (arcsec)	30	24
Integration time (min)	1	1

Table 3. ATCA observational parameters for G349.7+0.2.

Parameter	OH observations				H ₂ CO	CH ₃ OH
	Dec 1999	Nov 1998	Nov 1998	May 2001	May 2000	Apr 2002
Date	Dec 1999 Jun 2000					
Central frequency (MHz)	1666	4660	6030	6049	4829	6668
		4751	6035			
		4765				
Array configurations	1.5A, 6B	6D	6D	750A	1.5A	6A
Primary beam (arcmin)	≈ 33	≈ 10	≈ 10	≈ 10	≈ 10	≈ 10
Total bandwidth (MHz):						
spectral-line	8	4	4	4	4	4
continuum	128	128	128	–	–	–
No. of frequency channels:						
spectral-line	1024	1024	1024	2048	2048	2048
continuum	32	32	32	–	–	–
Velocity resolution (km s^{-1})	1.6	0.2	0.2	0.1	0.1	0.1
Total observing time (hr)	2×13	13	13	3	13	6
Spectral-line cubes:						
Synthesised beam (arcsec ²)	15×12	3×2	2×2	37×10	4×2	2×1.5
rms noise (mJy beam ⁻¹)	5	7	6	9	7	9

Table 4. Molecular transitions observed with ATCA towards G349.7+0.2.

Molecule	Frequency	Transition
OH	1665 MHz	$^2\Pi_{3/2} J=3/2$
OH	1667 MHz	$^2\Pi_{3/2} J=3/2$
OH	4660 MHz	$^2\Pi_{1/2} J=1/2$
OH	4751 MHz	$^2\Pi_{1/2} J=1/2$
OH	4765 MHz	$^2\Pi_{1/2} J=1/2$
OH	6031 MHz	$^2\Pi_{3/2} J=5/2$
OH	6035 MHz	$^2\Pi_{3/2} J=5/2$
OH	6049 MHz	$^2\Pi_{3/2} J=5/2$
H ₂ CO	4829 MHz	$1_{11} - 1_{10}$
CH ₃ OH	6668 MHz	$5_1 - 6_0 A^+$

Table 5. The first three columns list the observed molecular transitions and their frequencies (ν) towards the SEST peak position, except for the CS and H₂CO transitions which are obtained towards M1. The fourth column lists the SEST and Mopra FWHM beam size, the fifth gives the observed brightness temperature and rms noise (upper limits are 2σ values), while the last two columns list line velocities (v_{LSR}) and FWHM line widths (Δv_{LSR}).

Molecule	Transition	ν (GHz)	Beam Size (arcsec)	T_{mb} (K)	v_{LSR} (km s $^{-1}$)	Δv_{LSR} (km s $^{-1}$)
¹³ CO ^a	1–0	110.197	43	3.9 ± 0.2	16.4	2.7
¹² CO	2–1	230.538	23	12.5 ± 0.1	15.1	3.9
	1–0	115.271	45	14.0 ± 0.2	16.5	3.9
CS	5–4	244.935	21	<0.4	—	—
	3–2	146.969	34	0.45 ± 0.09	16.1	4.2
	2–1	97.981	52	0.26 ± 0.09	16.7	3.3
	3–2	267.557	20	<0.3	—	—
HCO ⁺	1–0	89.188	54	1.50 ± 0.08	13.3	4.5
	3–2	265.886	20	<0.5	—	—
HCN	1–0 ^b	88.632	55	0.75 ± 0.08	12.9	3.3
	3–2	225.698	23	<0.2	—	—
	3–2	218.222	24	<0.2	—	—
H ₂ CO	2–1–1–1(1,0)	150.498	36	0.26 ± 0.08	16.8	6.5
	2–1–1–1(1,1)	140.839	38	<0.2	—	—
	23–12	109.252	47	<0.2	—	—
	32–21	99.299	50	0.37 ± 0.09	14.7	3.0
SiO	5–4 v=0	217.105	24	<0.4	—	—
	3–2 v=0	130.268	40	<0.3	—	—
	2–1 v=0	86.846	57	<0.2	—	—

(a) from Mopra observations; (b) values for the main hyperfine component;

Table 6. Summary of results from UNSWIRF observations. The knots denote H₂ peaks near the five OH(1720 MHz) masers. Both sets of features are numbered correspondingly. The second and third columns list the peak flux density of 1–0 and 2–1 S(1) H₂ lines, corrected for extinction as follows: $A_{2.12} = 3$ mag, $A_{2.25} = 2.7$ mag. The fourth and fifth columns list the total flux density of corresponding H₂ lines, corrected for extinction. The sixth and seventh columns list the luminosity of the corresponding H₂ lines for source distance of 18 kpc. The eighth column gives the line ratio $R = L(1\text{--}0)/L(2\text{--}1)$. The absolute flux density measurements have $\approx 30\%$ uncertainty.

Designation	$F_p(1\text{--}0)$ ($\times 10^{-4}$ erg s $^{-1}$ cm $^{-2}$ sr $^{-1}$)	$F_p(2\text{--}1)$ ($\times 10^{-4}$ erg s $^{-1}$ cm $^{-2}$ sr $^{-1}$)	$F_{int}(1\text{--}0)$ ($\times 10^{-13}$ erg s $^{-1}$ cm $^{-2}$)	$F_{int}(2\text{--}1)$ ($\times 10^{-13}$ erg s $^{-1}$ cm $^{-2}$)	$L(1\text{--}0)$ (L_{\odot})	$L(2\text{--}1)$ (L_{\odot})	R
Knot 1	24	6.0	38	8.4	38	8	5
Knot 2	52	9.6	66	12	66	12	5
Knot 3	43	8.4	49	10	49	10	5
Knot 4	36	7.2	40	4.8	40	5	8
Knot 5	44	8.4	41	7.2	41	7	6
total	52	9.6	540	90	540	88	6

Table 7. Parameters of the main-line OH masers at 1665 and 1667 MHz detected towards the region of G349.7+0.2.

Parameter	MM(1)	MM(2)
RA (2000) (h m s)	17 17 59.3	17 18 11.1
Dec. (2000) (° ' '')	–37 26 10.00	–37 28 23.93
1665 peak (Jy)	0.09	0.06
1665 V _{peak} (km s $^{-1}$)	21	16
1667 peak (Jy)	–	0.10
1667 V _{peak} (km s $^{-1}$)	–	10

Table 8. Molecular column densities, $N(\text{mol})$, and abundances, $X=N(\text{mol})/N(\text{H}_2)$ for $N(\text{H}_2)=1.2\times10^{21} \text{ cm}^{-2}$, of the molecular cloud interacting with the SNR G349.7+0.2. For comparison, abundances of the shocked molecular gas in SNR IC 443 (van Dishoeck et al. 1993) are listed, as well as those of the dark clouds TMC-1 and L134N (Ohishi et al. 1992). Note that abundance values are always assumed for ^{12}CO and ^{13}CO .

Molecule	G349.7+0.2		IC 443 ^a		TMC-1		L134N	
	N (cm $^{-2}$)	X	X_1	X_2	X	X	X	X
^{12}CO	1.2×10^{17}	1×10^{-4}	10^{-4}	10^{-4}	8×10^{-5}	8×10^{-5}		
^{13}CO	2.4×10^{15}	2×10^{-6}	2×10^{-6}	2×10^{-6}		
HCO^+	1.2×10^{14}	9.8×10^{-8}	1×10^{-8}	3×10^{-10}	8×10^{-9}	8×10^{-9}		
HCN	5.2×10^{13}	4.3×10^{-8}	3×10^{-8}	9×10^{-9}	2×10^{-8}	4×10^{-9}		
CS	4.8×10^{13}	4.0×10^{-8}	6×10^{-9}	8×10^{-9}	10^{-8}	10^{-9}		
SO	1.5×10^{14}	1.2×10^{-7}		8×10^{-9b}	5×10^{-9}	2×10^{-8}		
H_2CO	$< 7\times10^{13}$	$< 610^{-8}$	7×10^{-9}	2×10^{-8}	2×10^{-8}	2×10^{-8}		
SiO	$< 3\times10^{13}$	$< 2\times10^{-8}$	$<2\times10^{-9}$	4×10^{-9}	$<2\times10^{-12}$	$<4\times10^{-12}$		

(a) Shocked gas in IC 443 is suggested to contain two components: X_1 abundances correspond to shocked gas with $n(\text{H}_2)\sim 10^5 \text{ cm}^{-3}$ and $T_{kin} \sim 80 \text{ K}$, while X_2 abundances correspond to shocked gas with $n(\text{H}_2)\sim 3\times10^6 \text{ cm}^{-3}$ and $T_{kin} \sim 200 \text{ K}$ (see van Dishoeck et al. 1993, for more details); (b) derived for a single component model;

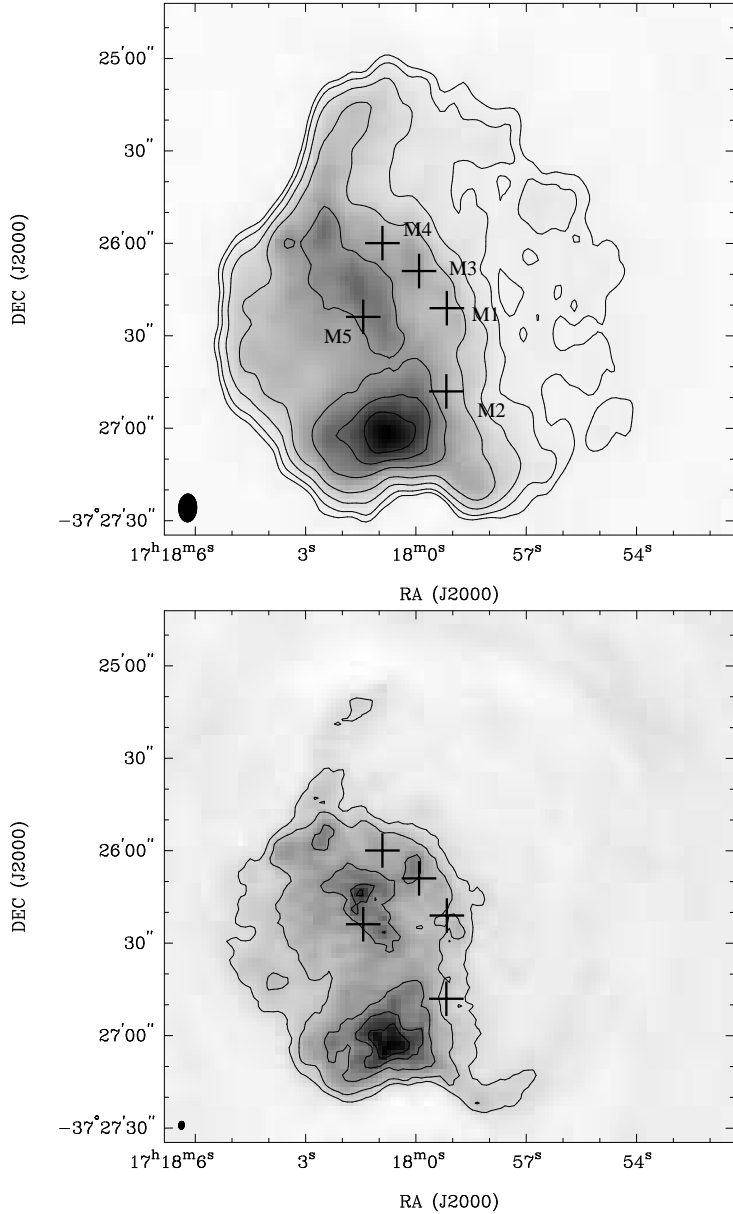


Figure 1. The ATCA continuum images of G349.7+0.2 at 18 cm (*top*) and 6 cm (*bottom*), shown in greyscale and contours. Contour levels are: (18 cm): 12, 17, 34, 68, 136, 204, 272 mJy beam⁻¹ and (6 cm): 1.6, 3.2, 6.4, 9.9, 12.8 mJy beam⁻¹. The crosses mark the OH(1720 MHz) maser positions. The synthesised beam is shown in the lower left corner.

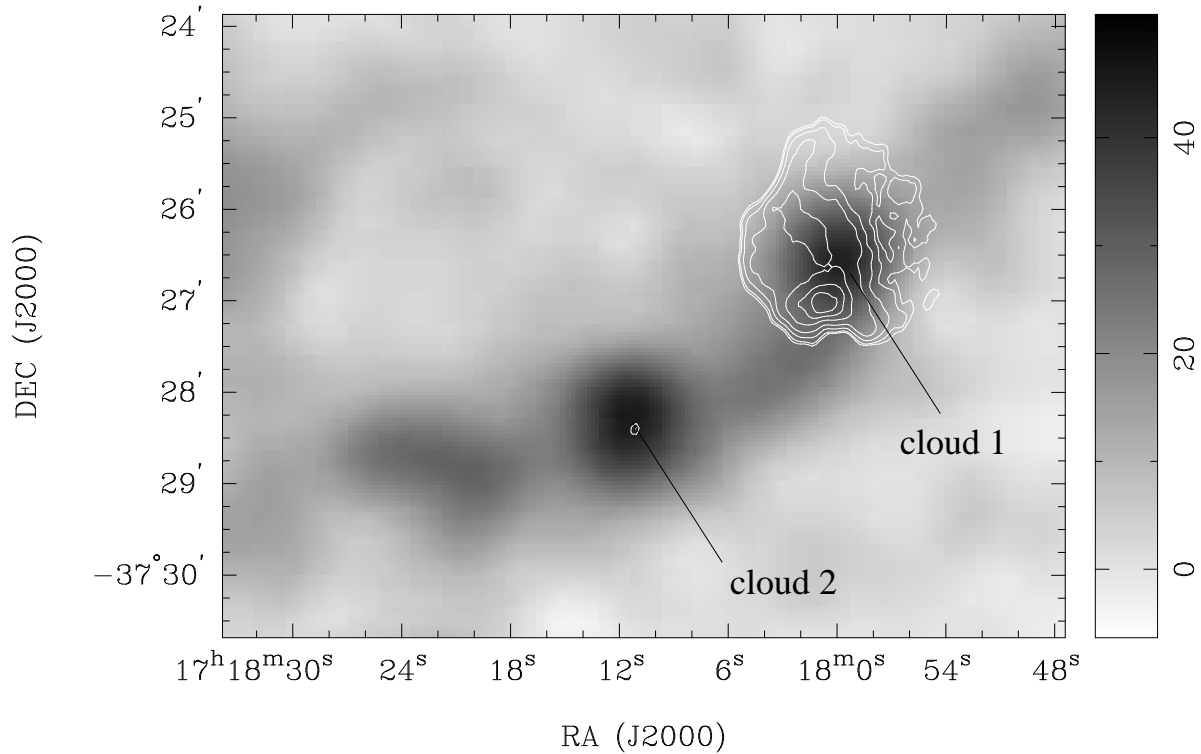


Figure 2. Greyscale image of the ^{12}CO 1–0 emission obtained with the 12-m NRAO (National Radio Astronomy Observatory) antenna, integrated between $+14.5$ and $+20.5$ km s^{-1} and convolved to a 60×60 arcsec^2 beam from Reynoso & Mangum (2001). The contours represents the 18 cm continuum emission from G349.7+0.2 with the levels same as in Figure 1. Cloud 1 is coincident with the SNR G349.7+0.2, and cloud 2 is coincident with an UC H II region IRAS 17147–3725 located to the southeast of the SNR, represented with a single radio contour.

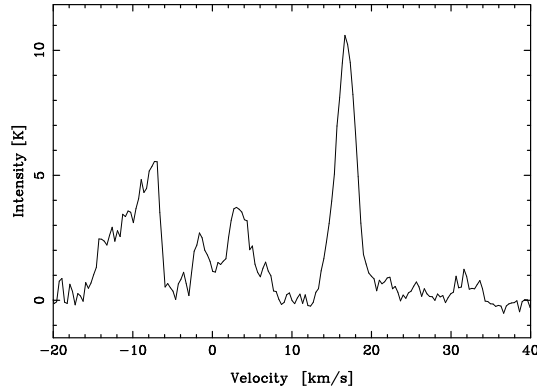


Figure 3. ^{12}CO 1–0 spectrum towards the SNR G349.7+0.2 in the range -20 to $+40 \text{ km s}^{-1}$. Molecular clouds are present at -10 km s^{-1} , $+6$ and $+16 \text{ km s}^{-1}$.

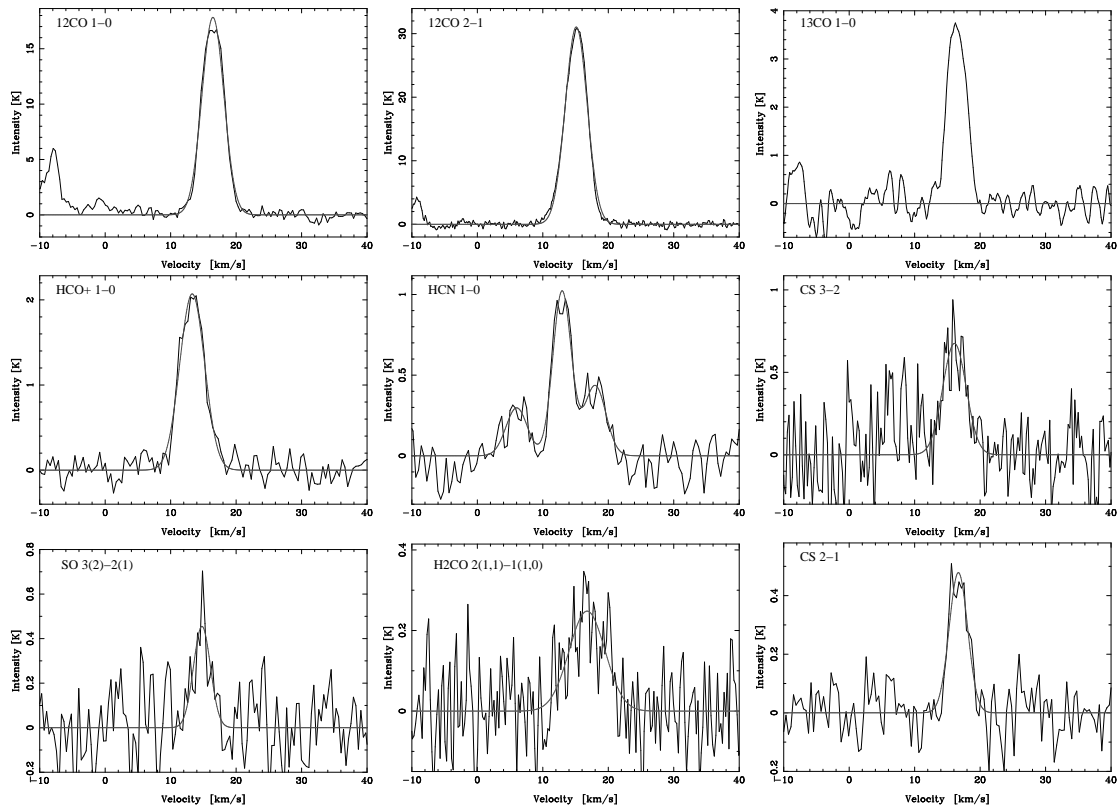


Figure 4. The observed millimetre-line profiles of the $+16 \text{ km s}^{-1}$ molecular cloud towards G349.7+0.2, overlaid with the Gaussian fit profiles. CS 3–2 and H_2CO $2_{(1,1)} - 1_{(1,0)}$ spectra are obtained towards the position of M1, while the other spectra are obtained towards the peak of the molecular cloud associated with the SNR.

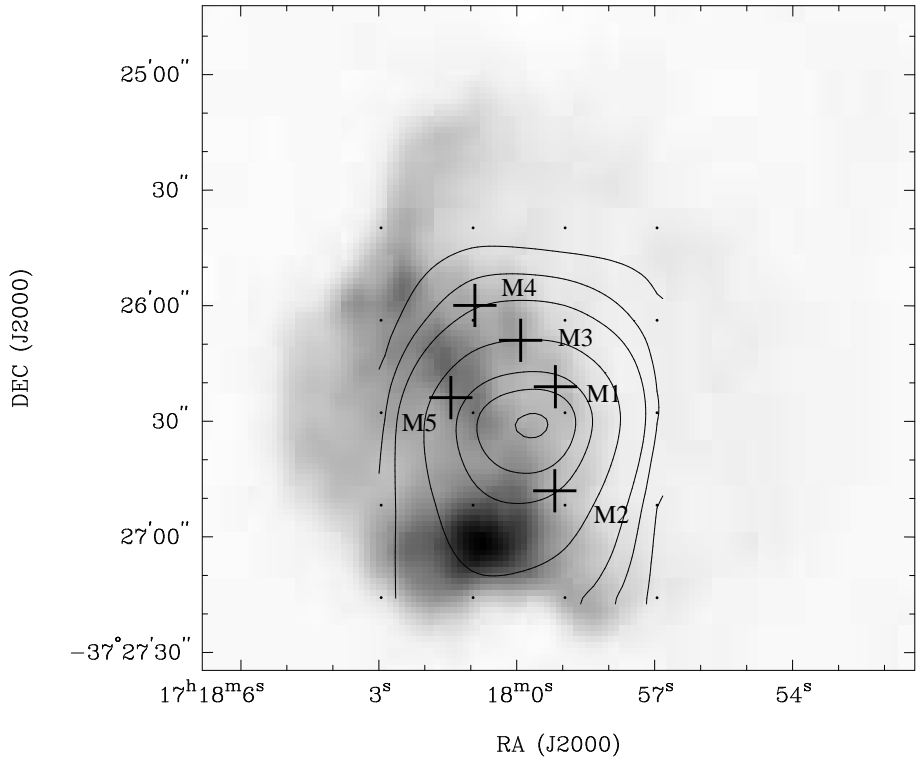


Figure 5. Contours of the velocity-integrated ($10\text{--}20 \text{ km s}^{-1}$) ^{12}CO 1-0 emission obtained with the SEST and overlaid on the 18 cm greyscale radio continuum obtained with the ATCA. The contour levels are: 16, 24, 32, 48, 63, 71, 78 K km s^{-1} . The dots mark the grid positions of the SEST observations. The crosses mark the OH(1720 MHz) maser positions.

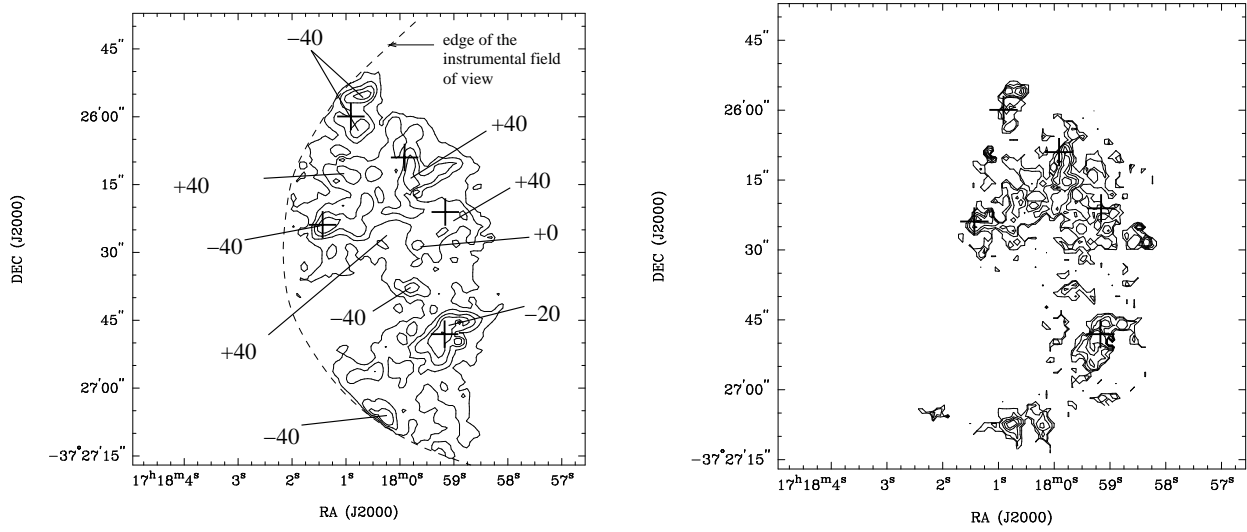


Figure 6. Contours of the velocity-integrated $2.12\text{ }\mu\text{m}$ H_2 1–0 S(1) line emission (left) and $2.25\text{ }\mu\text{m}$ H_2 2–1 S(1) line emission (right). Note that flux densities are not corrected for extinction (which is assumed to be a minimum 3 mag in K ($2.12\mu\text{m}$) band). The contours are for 1–0 S(1) emission: $3.3, 6.7, 13.2, 19.7$ and $26.3 \times 10^{-5}\text{ erg s}^{-1}\text{ cm}^{-2}\text{ sr}^{-1}$; for 2–1 S(1) emission: $2.7, 3.6, 4.5, 5.3$ and $6.2 \times 10^{-5}\text{ erg s}^{-1}\text{ cm}^{-2}\text{ sr}^{-1}$. The crosses mark the OH(1720 MHz) maser positions. Line-centre velocities of H_2 emission are also indicated in the left panel.

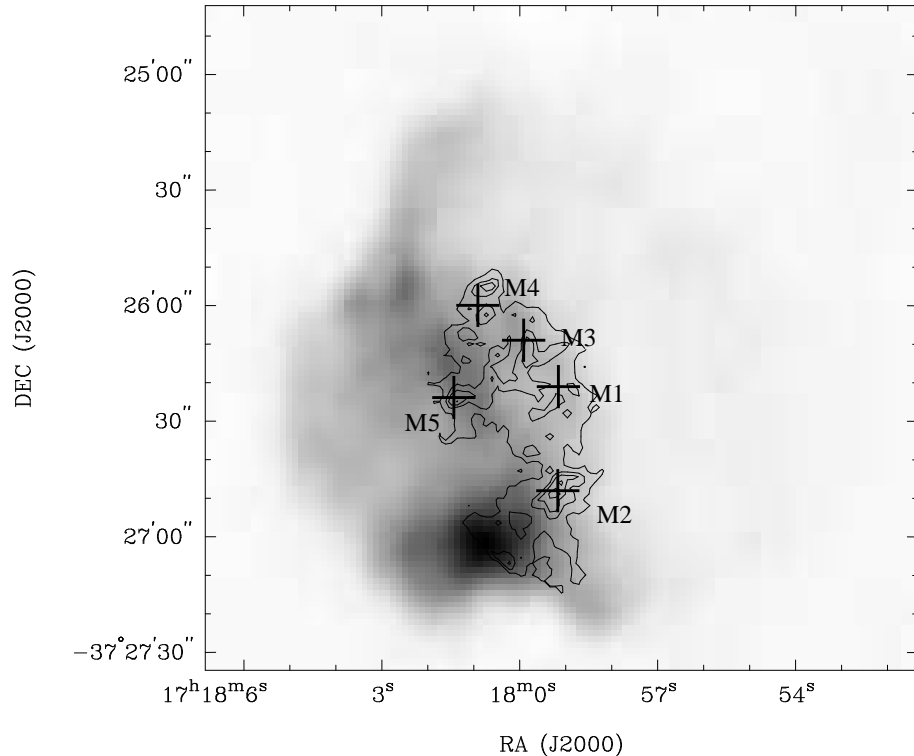


Figure 7. Contours of $2.12\text{ }\mu\text{m}$ H_2 1–0 S(1) emission overlaid on the 18-cm greyscale radio continuum image of G349.7+0.2. The contour levels (not corrected for extinction) are: $3.2, 9.6, 15.9$ and $25.5 \times 10^{-5}\text{ erg s}^{-1}\text{ cm}^{-2}\text{ sr}^{-1}$. The crosses mark the OH(1720 MHz) maser positions, which are again shown numbered.

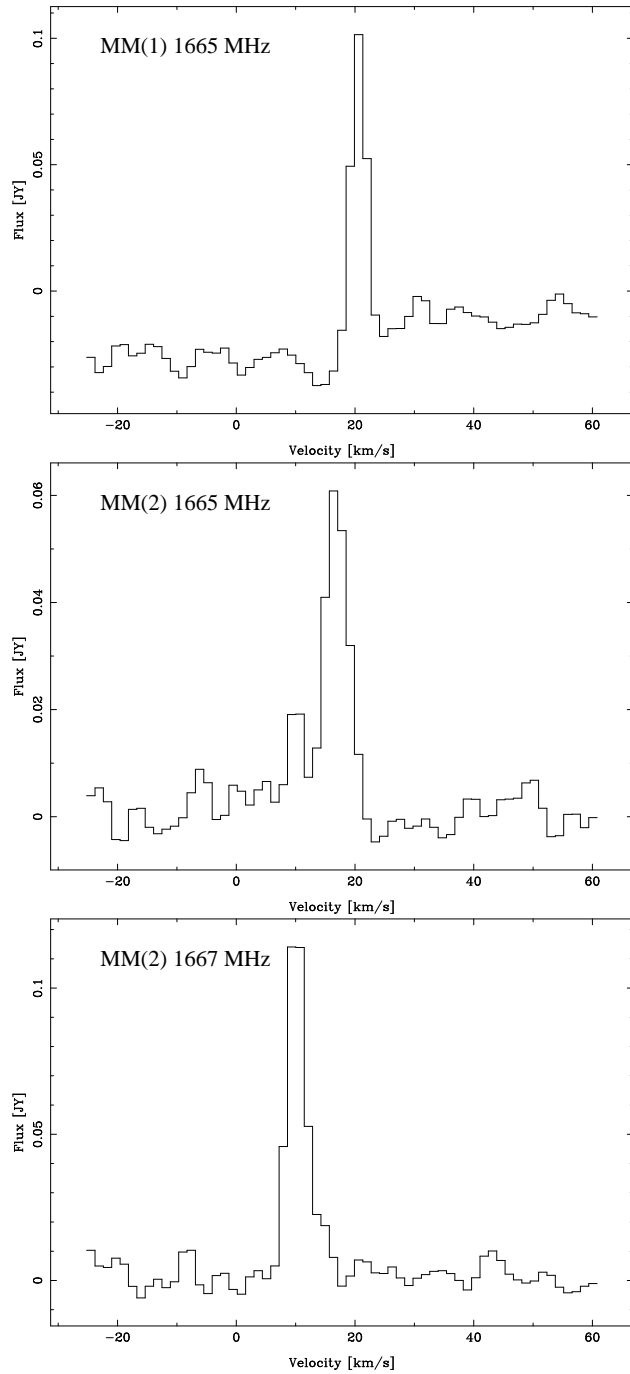


Figure 8. Main-line maser profiles towards two locations in G349.7+0.2. MM(1) is located within the SNR contours, and MM(2) originates from the UC H II region located southeast from the remnant.

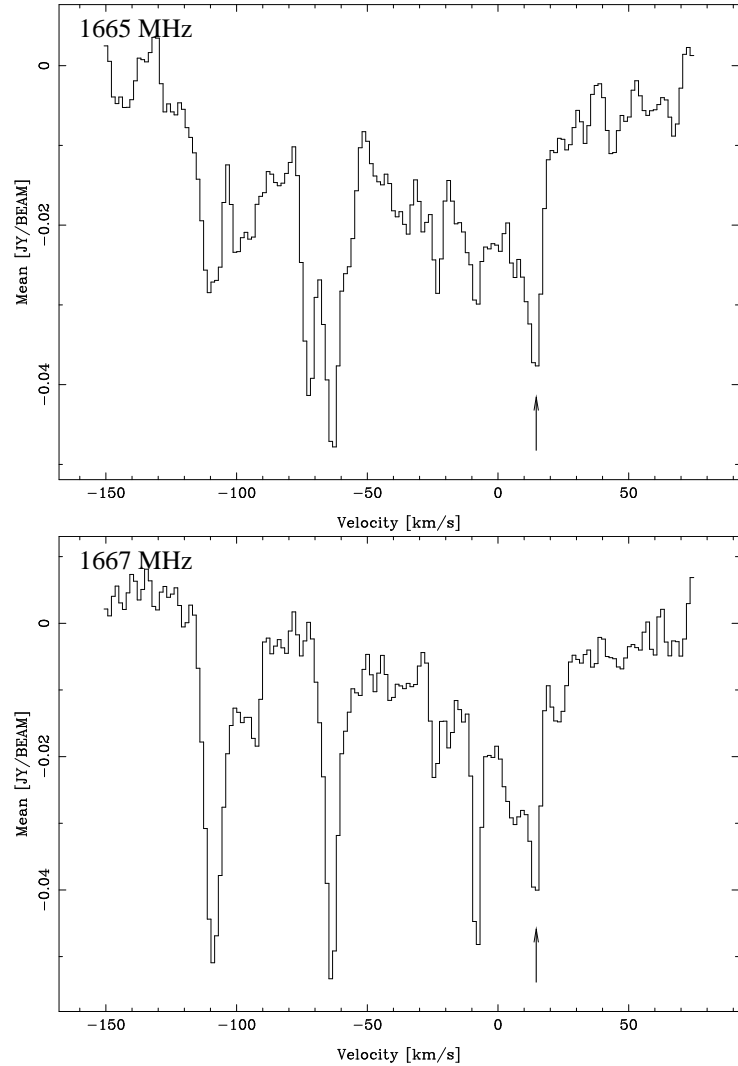


Figure 9. Line profiles of 1665 and 1667 MHz OH absorption, Hanning smoothed by 3 channels, show the features along the line of sight to the SNR G349.7+0.2. The arrow indicates the velocity of the material associated with the remnant.

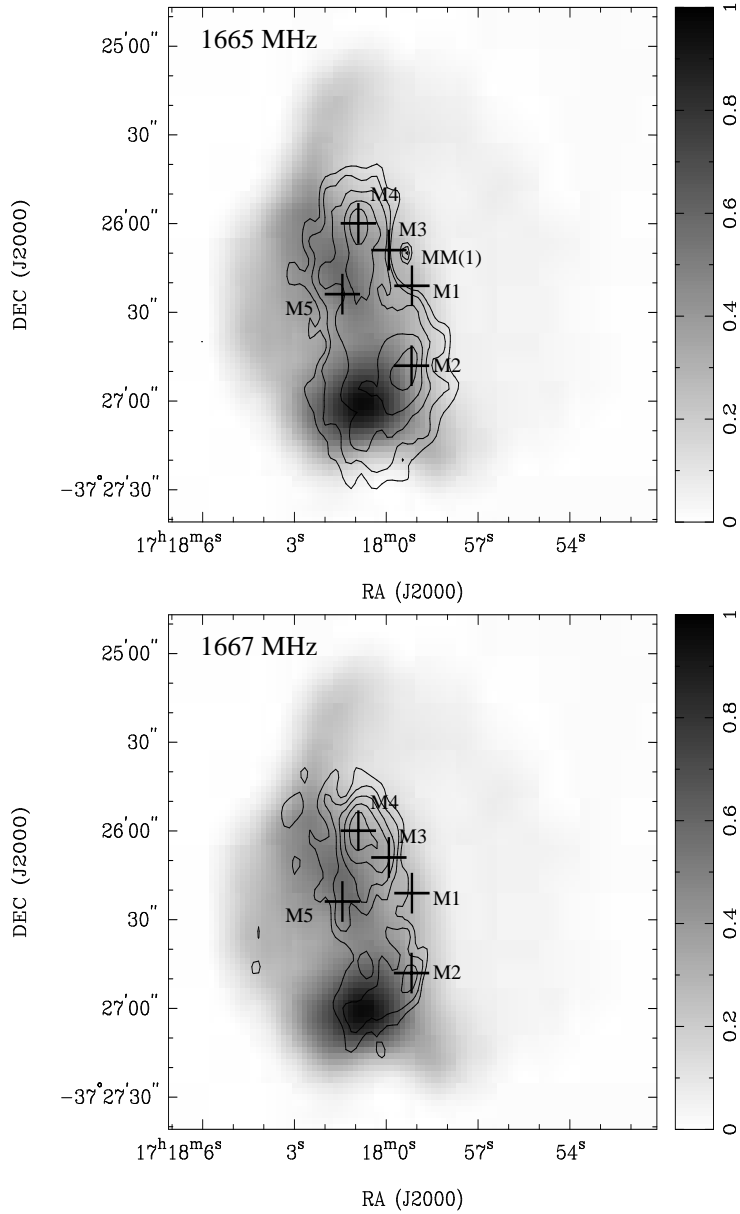


Figure 10. Contour images of the 1665 and 1667 MHz OH absorption, integrated between 10 and 20 km s^{-1} overlaid on the greyscale 18-cm continuum image of G349.7+0.2. The contours are: $-0.13, -0.16, -0.20, -0.25$ and -0.30 $\text{Jy beam}^{-1} \text{ km s}^{-1}$. The crosses mark the OH(1720 MHz) maser positions and the compact source in the 1665 MHz image is a compact OH(1665 MHz) maser, marked as MM(1).

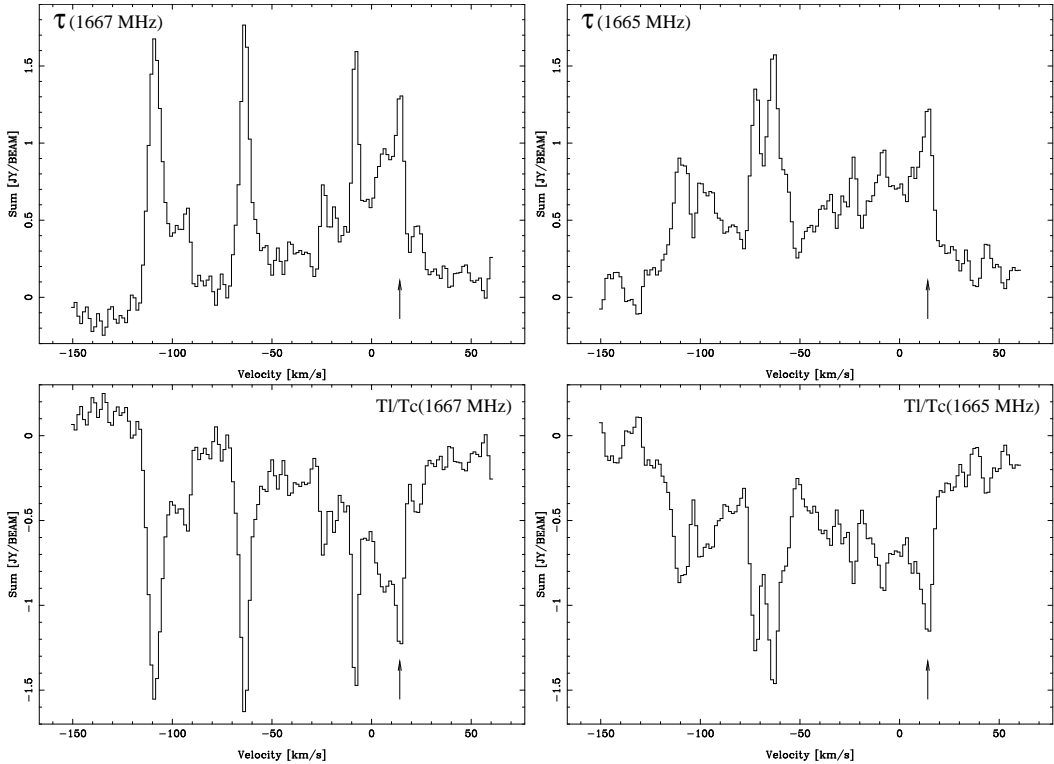


Figure 11. Line profiles of the 1665 and 1667 MHz OH optical depth (upper panels), and profiles of the line-to-continuum ratio (lower panels) towards the peak of the OH cloud. The spectra have been Hanning smoothed by 3 channels. The arrow indicates the velocity of the material associated with the remnant.

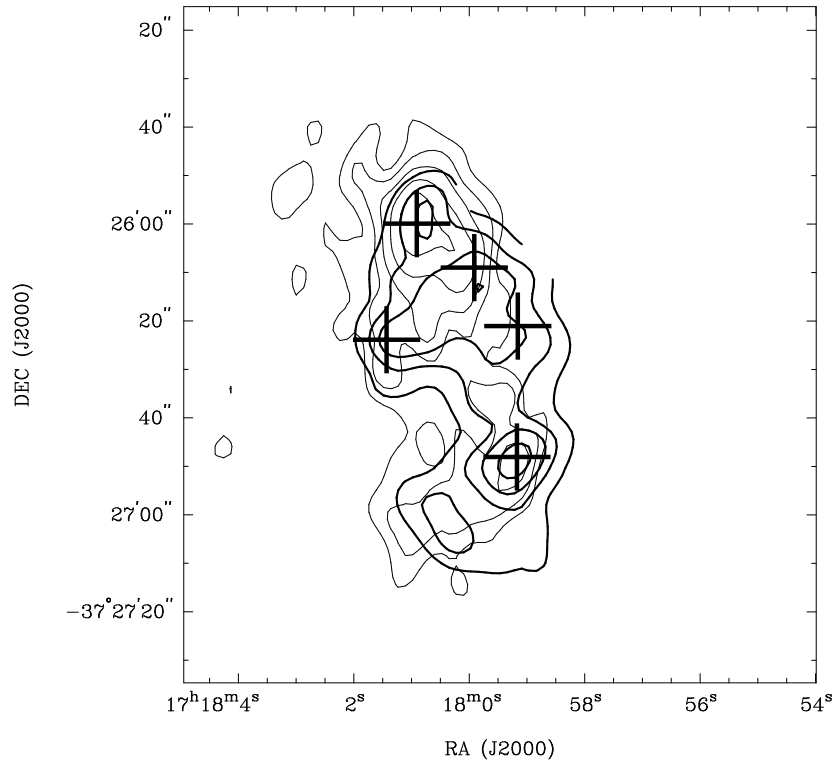


Figure 12. Contours of OH(1667 MHz) absorption distribution (light lines) superimposed on that of $2.12 \mu\text{m}$ H_2 1–0 S(1) emission (heavy lines) which have been convolved to a similar resolution. The two distributions show a good correlation. The OH contour levels are the same as in Figure 10, and the H_2 contour levels are: $3.4, 10.1, 16.9$ and $27.0 \times 10^{-4} \text{ erg s}^{-1} \text{ cm}^{-2} \text{ sr}^{-1}$. The crosses mark the OH(1720 MHz) maser positions.

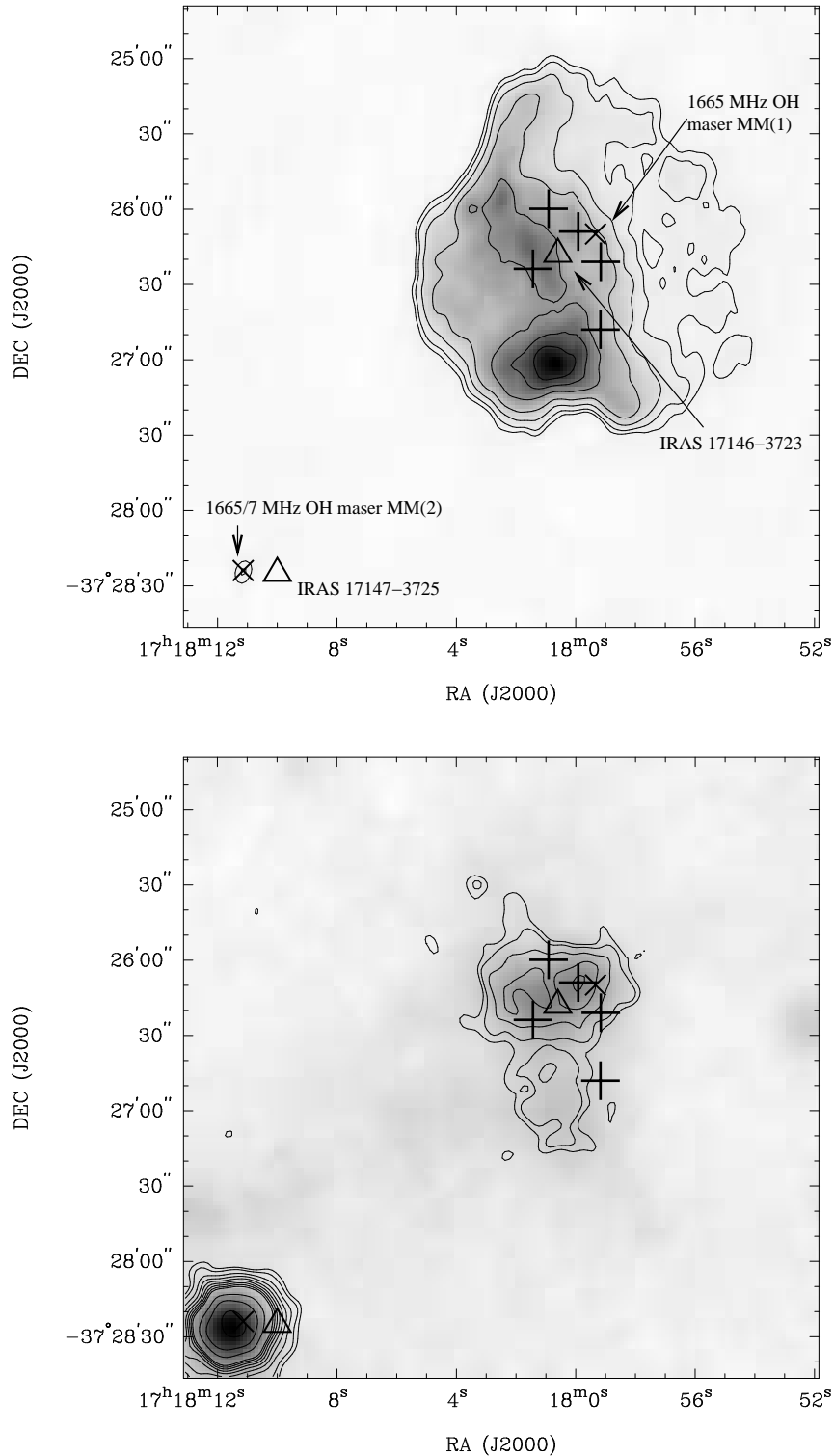


Figure 13. (Top:) Radio continuum image at 18 cm of G349.7+0.2 and the UC H II region IRAS 17147–3725 overlaid with the features found in the region: the + mark the OH(1720 MHz) maser positions, the \times mark the positions of main-line OH masers, and triangles mark positions of IRAS sources. Contour levels are same as in Figure 1. (Bottom:) MSX 8.3 μ m (greyscale) and 21.3 μ m (contours) emission. Contour levels are: 6, 7, 10, 12, 14, 17, 19, 22, 24, 36, 48, 72 and 96 $\times 10^{-6}$ W m $^{-2}$ sr $^{-1}$, and greyscale range is from 4.2×10^{-6} to 2.3×10^{-5} W m $^{-2}$ sr $^{-1}$.

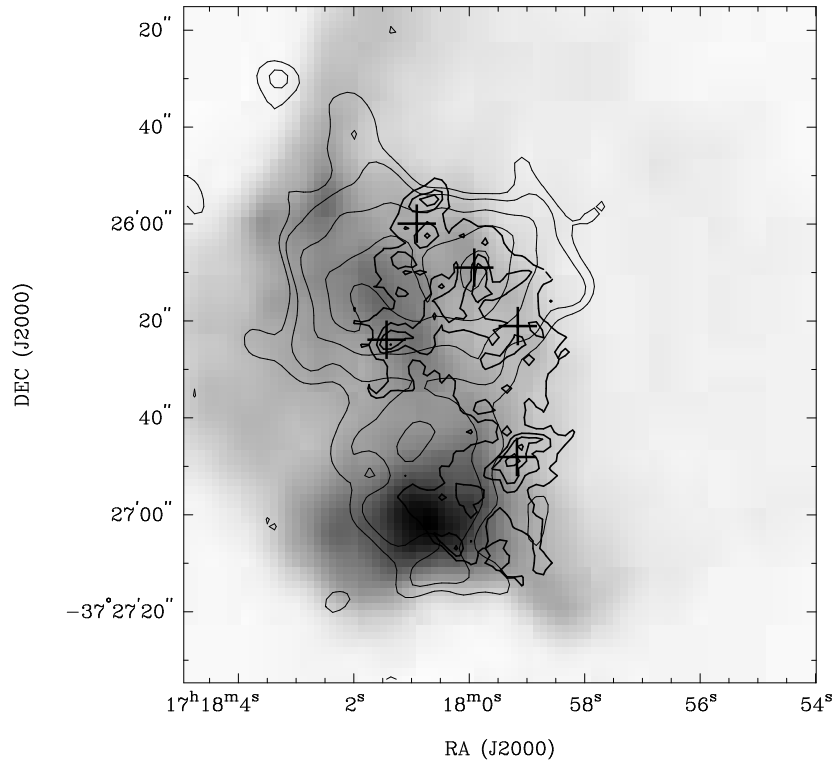


Figure 14. The 18-cm greyscale continuum image of G349.7+0.2 overlaid with MSX 8.3 μm (light contours) and H₂ (heavy contours) emission. The contour levels for the 8.3 μm emission are the same as Figure 13, and for H₂ emission, the same as in Figure 12. Note that the lowest H₂ levels in the south-east have been truncated by the instrumental field of view.